The Astrophysical Journal, 887:77 (25pp), 2019 December 10 https://doi.org/10.3847/1538-4357/ab521f

Modeling Energetic Particle Acceleration and Transport in a Solar Wind Region with Contracting and Reconnecting Small-scale Flux Ropes at Earth Orbit

J. A. Le Roux[1,2], G. M. Webb[2], O. V. Khabarova[3], L.-L. Zhao[2], and L. Adhikari[2]
[1] Department of Space Science, University of Alabama in Huntsville, Huntsville, AL 35805, USA; jar0013@uah.edu
[2] Center for Space Plasma and Aeronomic Research (CSPAR), University of Alabama in Huntsville, Huntsville, AL 35805, USA
[3] Heliophysical Laboratory, Pushkov Institute of Terrestrial Magnetism, Ionosphere and Radiowave Propagation RAS (IZMIRAN), Troitsk, Moscow 142190, Russia
Received 2019 September 2; revised 2019 October 25; accepted 2019 October 27; published 2019 December 11

Abstract

New analytical steady-state and time-dependent solutions for the acceleration of energetic particles by contracting and reconnecting small-scale flux ropes (SMFRs) in the solar wind are presented. For this purpose, a telegrapher-type Parker transport equation was derived from the existing underlying focused transport equation. The solutions unify all SMFR acceleration mechanisms present in the transport equation, showing that SMFR acceleration by the reconnection electric field in the mixed-derivative transport term is constrained by and requires the presence of second-order Fermi SMFR acceleration. We explore the potential of these solutions in reproducing energetic proton flux enhancements and spectral evolution between ∼50 keV and 5 MeV in dynamic SMFR regions near large-scale reconnecting current sheets in the solar wind at Earth orbit. It is shown that second-order Fermi SMFR acceleration involving the variance in SMFR compression and incompressible parallel shear flow and confirmed that first-order SMFR Fermi acceleration, due to mean SMFR compression (successfully used before in data fits), are both workable options in reproducing observed flux amplification factors when using reasonable SMFR parameters. However, the predicted substantial quantitative differences in the spatial evolution of the accelerated spectra through the SMFR region might provide a way to distinguish between first- and second-order Fermi SMFR acceleration in observations. It is concluded that more detailed data analysis of SMFR parameters in SMFR acceleration events is needed before the relative role of first- and second-order SMFR acceleration mechanisms can be determined.

Unified Astronomy Thesaurus concepts: Solar energetic particles (1491); Solar magnetic reconnection (1504); Solar wind (1534); Solar magnetic fields (1503)

1. Introduction

Discoveries made in recent years strengthen the case for a new paradigm whereby energetic particle acceleration events, not associated with diffusive shock acceleration (DSA) by interplanetary shocks in the solar wind, can be explained in terms of particle acceleration in solar wind regions filled with dynamic, interacting small-scale magnetic flux ropes (SMFRs). SMFRs are defined as quasi-helical coherent nonlinear magnetic field structures advected with the solar wind flow that are composed of a twist or magnetic island component and an axial or guide field component (Cartwright & Moldwin 2010). These structures are typically observed to have cross sections $\leqslant$0.01 au at 1 au, basically coinciding with the inertial and dissipation range of magnetic turbulence, but there have been some mention of larger values between ∼0.01 and 0.1 au (Cartwright & Moldwin 2010; Khabarova et al. 2015; Hu et al. 2018). These structures should be distinguished from pseudo-flux ropes such as torsional Alfvén waves which propagate at the Alfvén speed in the solar wind frame (e.g., Hu et al. 2018). Especially noteworthy is observational evidence for the following: (i) local production of SMFRs through turbulent magnetic reconnection at strong, large-scale (primary) current sheets in the solar wind such as the disturbed (rippled) heliospheric current sheet (HCS) and current sheets associated with interplanetary coronal mass ejections (ICMEs) and corotating interaction regions (CIRs). Populations of dynamic SMFRs confined in regions bounded by such current sheets are generated when, e.g., CIRs and ICMEs interact, traveling shocks interact with the HCS, or ripples form in the disturbed HCS (Khabarova et al. 2015, 2016; Adhikari et al. 2019). From an MHD turbulence perspective, such collections of SMFRs are interpreted as a manifestation of dynamic interacting quasi-2D MHD turbulence (Zank et al. 2017). (ii) Strong enhancements in energetic ion flux up to MeV/nuc energies and in energetic electron flux up to ∼50 keV, and the development of accelerated energetic ion spectra that become increasingly hard with distance inside SMFR regions due to a spectral bend-over at lower energies (Zank et al. 2015; Khabarova & Zank 2017; Zhao et al. 2018; Adhikari et al. 2019).

Alternatively, there is the longstanding view that, in the presence of a significant guide/background magnetic field, an intrinsically incompressible quasi-2D MHD turbulence component of magnetic islands naturally emerges as the dominant dynamic turbulence component perpendicular to the guide/background magnetic field in the solar wind. This view is supported by solar wind observations near 1 au (e.g., Matthaeus et al. 1990; Bieber et al. 1994), MHD simulations (e.g., Shebalin et al. 1983; Dmitruk et al. 2004), and nearly incompressible solar wind MHD turbulence theory (Zank & Matthaeus 1992, 1993; Hunana & Zank 2010; Zank et al. 2017) in which Alfvén wave turbulence forms is a minor secondary turbulence component. Recent identification of SMFRs in unprecedented numbers using Grad–Shrafanov reconstruction techniques at 1 au (Hu et al. 2018; Zheng & Hu 2018) supports the view of nearly incompressible turbulence theory and simulations that SMFRs should be continuously present in the solar wind near 1 au. Because the analysis shows that the number of SMFRs peak in the vicinity of primary reconnecting current sheets (see also Cartwright & Moldwin 2010), this

viewpoint suggests large-scale current sheets act as additional local sources of SMFR turbulence. The identified SMFRs also yield axial-current density statistical profiles capturing the intermittent nature of quasi-2D turbulence in MHD turbulence simulations (Zheng & Hu 2018).

Irrespective of the origin of SMFRs, evidence from simulations suggests efficient acceleration of charged particles traversing regions filled with dynamic SMFRs that can result in power-law spectra for energetic particles as first pointed out by Matthaeus et al. (1984) and Ambrosiano et al. (1988), and confirmed later by many others (Dmitruk et al. 2004; Drake et al. 2006, 2013; Li et al. 2015, 2017, 2018, for example). Theoretical explanation of the main acceleration mechanisms in the simulations often rely on the first and second adiabatic invariants combined with magnetic flux conservation (e.g., Drake et al. 2006, 2013; Zank et al. 2014), guiding center kinetic transport theory (e.g., Dahlin et al. 2016, 2017), and its close cousin, focused transport theory (Le Roux et al. 2015, 2018; Li et al. 2018). These approaches, besides providing familiar nonresonant acceleration concepts for SMFRs, also show promise in reproducing simulation results on macro scales. where the limitation of nearly gyrotropic particle phase angle distributions is less problematic. This opened up the possibility that these kinetic transport theories can be used to model particle acceleration by SMFRs on large scales in the solar wind, which is computationally beyond the reach of full particle simulations especially.

This led Zank et al. (2014) and Le Roux et al. (2015, 2018) to develop kinetic focused transport theories that unify the main nonresonant SMFR acceleration mechanisms identified in simulations. Expressed in terms of guiding center kinetic theory, the main acceleration mechanisms are (i) parallel guiding center motion acceleration by the parallel reconnection electric field generated when neighboring SMFRs form secondary reconnecting current sheets between them that merge (e.g., Oka et al. 2010), (ii) curvature drift acceleration by the motional electric field generated in SMFRs that contract or merge (e.g., Drake et al. 2006, 2013; Li et al. 2017, 2018), and (iii) Lagrangian betatron acceleration, which is based on magnetic moment conservation when the magnetic field strength in the plasma drift flow frame slowly varies in time and space. This mechanism includes grad-B drift acceleration by the motional electric field generated in contracting and merging SMFRs (e.g., Dahlin et al. 2016, 2017). In focused transport theory, the same acceleration mechanisms manifest in terms of nonuniform plasma flow effects. In this context, the main SMFR acceleration mechanisms identified in particle simulations are SMFR compression acceleration and SMFR incompressible parallel shear-flow acceleration (parallel component of the SMFR shear-flow tensor in the limit of divergence-free SMFR flow), while acceleration by the parallel reconnection electric field is the same as in guiding center kinetic theory (Zank et al. 2014; Le Roux et al. 2015, 2018; Li et al. 2018). Having studied how the SMFR acceleration mechanisms in focused transport theory and guiding center kinetic transport theory are connected, Le Roux et al. (2018) concluded that (i) SMFR compression acceleration can be viewed as a combination of curvature drift momentum gain by the motional electric field induced by magnetic island compression with Lagrangian betatron momentum gain (momentum gain from unified betatron and grad-B drift acceleration), due to the increasing magnetic field strength resulting from magnetic island compression when the magnetic-island-containing area shrinks as a result of the compression. (ii) SMFR incompressible parallel shear-flow acceleration can be interpreted as the combination of curvature drift momentum gain in the motional electric field generated by magnetic island contraction or merging with competing Lagrangian betatron momentum loss (momentum loss from unified betatron and grad-B drift acceleration) from the decreasing magnetic field strength resulting from magnetic island contraction or merging, during which the magnetic-island-containing area is conserved. (iii) Focused transport theory also includes an acceleration mechanism to refer to parallel guiding center motion momentum gain or loss from the noninertial force associated with the parallel component of acceleration of the plasma flow in SMFRs (Le Roux et al. 2018). This mechanism can be traced back as being part of the guiding center kinetic theory acceleration term describing the effect of the electric field on drift inertia (the part that refers to the acceleration of the parallel guiding center $d(v_{\parallel}\boldsymbol{b})/dt$ that also is the source of the curvature drift acceleration mechanism).

From the SMFR focused transport equations, diffusive Parker-type transport equations were derived assuming that on large spatial scales in the solar wind pitch-angle scattering will inevitably result in near-isotropic energetic particle distributions. Accordingly, the distributions were expanded out to the second anisotropic moment (Zank et al. 2014; Le Roux et al. 2015). From these equations, it became clear that SMFR compression acceleration, first advocated by Zank et al. (2014) and later also by Le Roux et al. (2015), Li et al. (2018), Du et al. (2018), can be considered as the only true first-order Fermi SMFR acceleration mechanism. In the focused transport equation, SMFR compression acceleration is a first-order Fermi acceleration mechanism because particles experience only energy gain as explained above. However, in the Parker transport limit, compression acceleration manifests as a combination of first-order and second-order Fermi acceleration, the former involving the isotropic moment of the distribution function and the latter associated with the second anisotropic moment of the particle distribution (Le Roux et al. 2018). Because the isotropic part of the distribution function is by far the dominant term in the expansion, first-order Fermi acceleration dominates SMFR compression acceleration in the Parker transport limit, which is consistent with SMFR compression acceleration in the underlying focused transport equation. SMFR incompressible parallel shear-flow acceleration, on the other hand, is intrinsically a second-order Fermi acceleration mechanism during significant pitch-angle scattering with net acceleration originating from the second anisotropic moment of the particle distribution. SMFR parallel guiding center motion acceleration by both the parallel reconnection electric field force and by the parallel component of the noninertial force associated with the acceleration of the plasma flow also yield second-order Fermi acceleration, but with the difference that net acceleration comes from the first anisotropic moment of the particle distribution. Thus, for a purely isotropic particle distribution, only first-order Fermi SMFR acceleration will be operative, while the other mechanisms need a particle distribution with a pitch-angle anisotropy to yield a net acceleration effect (see also Drake et al. 2010).

2. Motivation and Approach

Analytical one-dimensional (1D) steady-state solutions of diffusive Parker transport equations for SMFR acceleration showed promise in qualitatively reproducing the observed features of energetic particle acceleration in SMFR regions in the solar wind as discussed above in the first paragraph of the previous section (Zank et al. 2014, 2015; Le Roux et al. 2015, 2016). Recently, Zhao et al. (2018) and Adhikari et al. (2019) reproduced remarkably well the features of accelerated energetic ion observations in SMFR regions at 5 au and 1 au, respectively, by focusing on two SMFR acceleration mechanisms, namely, first-order Fermi acceleration (mean SMFR compression acceleration) and parallel guiding center motion acceleration by the mean parallel reconnection electric field generated at secondary (small-scale) reconnecting current sheets in merging SMFRs. The latter mechanism is represented by a mixed spatial and momentum derivative term in the Parker transport equation and was discussed first in Zank et al. (2014). It appears that first-order Fermi acceleration was the dominant process, because otherwise it would not have been possible to generate particle flux enhancements (Zank et al. 2014). An important element in the success of this approach was the addition of a loss term due to particle escape from the SMFR region that yielded more realistic steeper accelerated particle spectra. This modeling approach, however, did not address the role of second-order Fermi acceleration by SMFRs and specified propagation and acceleration timescales without making a connection to SMFR parameters, which admittedly are not well known.

In this publication, we extend previous analytical solutions of the Parker transport equation for SMFR acceleration in Zank et al. (2014), Le Roux et al. (2015), Zhao et al. (2018), and Adhikari et al. (2019) by presenting new 1D analytical solutions that combine first-order Fermi SMFR acceleration, acceleration by the SMFR parallel reconnection electric field due to the mixed-derivative transport term, and second-order Fermi SMFR acceleration for the various SMFR acceleration mechanisms. Thus, we unify all of the SMFR acceleration mechanisms in the underlying focused transport theory in a solution involving the Parker transport limit of the theory. Furthermore, besides steady-state solutions, we present new time-dependent analytical solutions. For this purpose, we derived a new telegrapher Parker transport equation from the underlying SMFR focused transport equation valid up to the second anisotropic moment of the particle distribution. A simplified, diffusive time-dependent solution ignoring telegrapher effects that can be compared to the steady-state solution at late times is also presented.

Armed with these solutions, we explore the possibility of reproducing observations of accelerated energetic ion flux enhancements and spectral evolution in active SMFR regions with reasonable SMFR parameters in the vicinity of 1 au, and whether one can, with current knowledge of SMFRs at 1 au, distinguish between contributions of different competing SMFR acceleration mechanisms. For this purpose, we use as a guide recent observations of energetic ion acceleration and propagation in SMFR regions as presented in Khabarova & Zank (2017) and Adhikari et al. (2019). Furthermore, we investigate whether second-order Fermi acceleration, generated when scattering energetic particles respond to statistical fluctuations in SMFR fields, can potentially reproduce the observations at 1 au when specifying reasonable SMFR parameters.

3. Observations of Energetic Particle Flux Enhancement in SMFR Regions at Earth Orbit

Despite magnetic reconnection being recognized as one of the most efficient processes for particle acceleration in space plasmas, it was generally thought that magnetic reconnection in the solar wind cannot result in efficient particle acceleration (see the main arguments in Gosling et al. 2005 and Fu et al. 2013). The reason for this misconception can be attributed to the adherence to the classical view of magnetic reconnection at current sheets in the heliosphere that led to data analysis on insufficient timescales to detect signs of particle acceleration associated with reconnection. Magnetic reconnection in interplanetary space was thought to be occurring locally at a certain point in a basically undisturbed primary (large-scale) current sheet without filamentation occupying a thin volume (Petschek-type reconnection). It was not considered that, because of turbulence in the solar wind, strong primary current sheets can also have a filamentary structure with complicated topology so that reconnection occurs in a turbulent fashion at multiple reconnection sites over a much broader and larger volume. Furthermore, turbulent reconnection produces numerous SMFRs in the vicinity of the filamentary current sheet so that reconnection at secondary (small-scale) current sheets between SMFRs occurs over a large volume (see Lazarian et al. 2012; Li & Lin 2012; Zharkova & Khabarova 2012; Eriksson et al. 2014; Egedal et al. 2015; Xia & Zharkova 2018). Operating within a broader conceptual framework of magnetic reconnection in the solar wind in which turbulence can also play a role, Khabarova & Zank (2017) revisited the key reconnection event presented by Gosling et al. (2005) as an example of inefficient particle acceleration associated with magnetic reconnection in the solar wind. By considering data on longer timescales associated with a much larger spatial volume relative to this reconnection event than Gosling et al. (2005), they discovered local particle acceleration up to MeV energies as a consequence of magnetic reconnection at a number of primary current sheets generating numerous SMFRs in between. To confirm the result statistically, Khabarova & Zank (2017) performed data analysis of the energetic particle flux detected by the Electron, Proton, and Alpha Monitor (EPAM) on board the *ACE* spacecraft based on 126 isolated narrow reconnection exhaust events compiled by Jack Gosling, who was looking for signatures of Petschek-like magnetic reconnection. By expanding the data analysis over longer timescales relative to these primary current events without significant distortion (occupying a thin volume), ample new evidence for efficient particle acceleration of both ions and electrons were found in their vicinity. Little acceleration was detected more locally to these current sheet events, in agreement with the findings of Gosling. It was concluded that by implication, only narrow reconnection outflows (exhausts) occurring in the closest vicinity of thin volume primary current sheets were taken into consideration by Gosling et al. (2005), while signatures of turbulent magnetic reconnection that occur in the solar wind at distorted primary current sheets in broader regions and at the secondary current sheets between larger SMFRs over much larger areas were not considered (see explanations in Khabarova & Zank 2017). Because thin reconnection exhausts of Petschek type are usually observed only at edges of large-scale regions, such as magnetic clouds, inside which turbulent reconnection occurs and numerous magnetic islands merge (reconnect) to generate clouds of accelerated particles (see Lazarian et al. 2012;

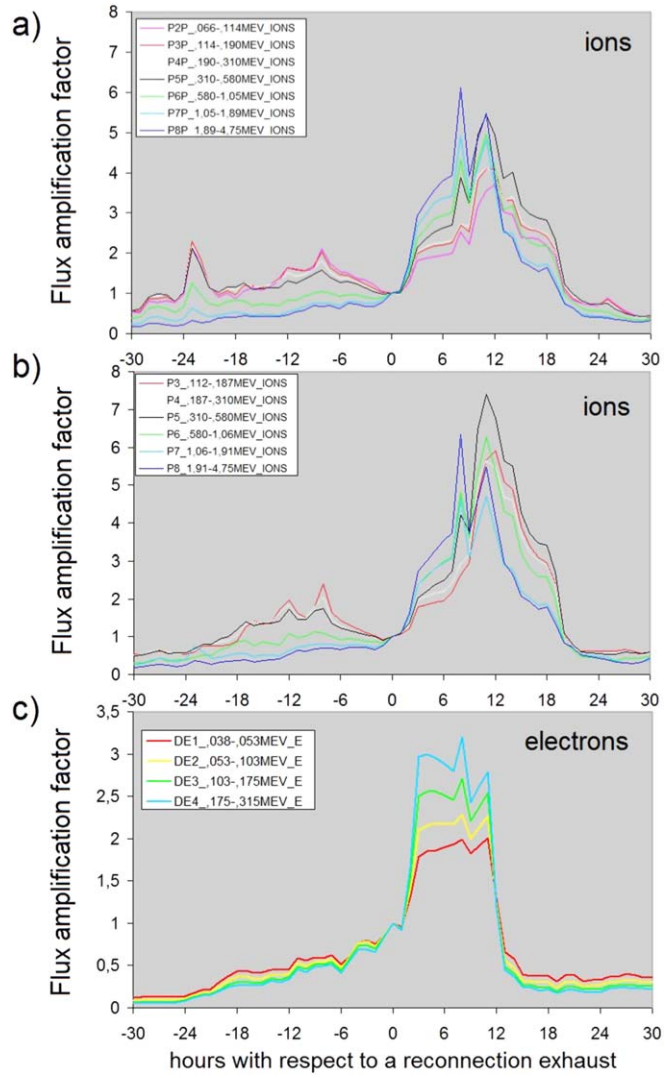

Figure 1. Variations of the averaged energetic particle flux amplification factor with respect to reconnection exhausts (primary current sheets) detected by the *ACE* spacecraft according to a superposed epoch analysis from Khabarova & Zank (2017) involving 126 Petschek-type reconnection exhaust events. Zero hour corresponds to the occurrence of each reconnection exhaust at which the flux amplification factor is normalized to a value of 1. From the *ACE* Electron, Proton, and Alpha Monitor (EPAM), we display from top to bottom the energetic ion flux from the LEMS120 telescope in (a) and the LEMS30 detector in (b), and energetic electron flux measurements from detector CA60 in (c).

Li & Lin 2012; Zharkova & Khabarova 2012; Eriksson et al. 2014; Egedal et al. 2015; Xia & Zharkova 2018), this particular method of current sheet identification led to the result that the energetic particle flux does not mainly peak at these relatively undisturbed primary reconnecting current sheets, but several hours after their passage (see Figures 10 and 11 of Khabarova & Zank 2017).

Figure 1 combines key panels of Figures 10 and 11 of Khabarova & Zank (2017), showing the flux amplification factor based on observations of the energetic ion flux from the LEMS120 telescope, which looks approximately in the magnetospheric direction (Figure 1(a)), its twin LEMS30, which looks approximately sunward (Figure 1(b)), and CA60, which measures electrons deflected from LEMS30 (Figure 1(c)). A flux amplification factor data analysis method has been introduced for the first time by Zank et al. (2015) and further employed in many studies probing the nature of particle acceleration in the solar wind (Khabarova & Zank 2017; Khabarova et al. 2017; Zhao et al. 2018; Adhikari et al. 2019; Malandraki et al. 2019). If particles are accelerated by interplanetary shocks, the amplification factor normalized to the energetic particle flux value at the position of the shock should be 1, slowly decreasing downstream. However, this expectation is often not met when the amplification factor grows to values much larger than one far downstream of interplanetary shocks, which indicates the existence of additional sources of particle energization (see also a detailed explanation of the flux amplification factor method in Malandraki et al. 2019). Zank et al. (2015) and Khabarova et al. (2016) showed theoretically that the energetic particle flux of classical DSA combined with downstream acceleration in dynamical SMFRs can potentially reproduce the amplification factor growth profile of higher-energy ions as a function of particle energy. This includes reproducing the trend that the particle flux amplification factor increases with particle energy. In the case of lower-energy particles below $\sim$5 MeV/nuc for ions (see Figure 1; Zhao et al. 2018 and Adhikari et al. 2019), the energetic particle flux downstream of the leading-edge ICME current sheet is dominated by particles accelerated inside the ICME structure with little contamination from particles that were accelerated locally at the preceding interplanetary shock. The effective diffusion length scale of the shock-accelerated particles is simply too short to enter the ICME structure (Zhao et al. 2018). Therefore, particle acceleration by SMFRs at lower energies can be modeled in isolation from DSA. Consequently, it is more practical to normalize the flux amplification factor of energetic particles at lower energies to a value of 1 at the leading-edge current sheet of the ICME, as was done in Figure 1 (see also Zhao et al. 2018), or at other current sheets inside the ICME structure (Adhikari et al. 2019) instead of at the shock. Thus, amplification factors larger than 1 indicate flux amplification whereas values less than 1 imply a flux decrease relative to the current sheet in question. In this way, the observation that the flux amplification factor increases with particle energy at higher particle energies was also confirmed in observations at lower energies, which further established this feature as a key signature of SMFR acceleration. Because the emphasis in this paper is on modeling the SMFR acceleration of suprathermal ions with energies below $\sim$5 MeV/nuc guided by the observations displayed in Figure 1, it is assumed that the DSA of particles by preceding interplanetary shocks can be ignored as a first approximation.

The growth of the flux amplification factor indicating active acceleration of both ions and electrons downstream of the identified reconnecting current sheets (as seen in Figure 1) generally correspond to the following two scenarios: (i) energization of particles within a strongly distorted ICME, in which a Petschek-type reconnecting current sheet at the leading edge of the ICME sheath and the fragmented magnetic cloud are followed by a series of strong current sheets separating dynamic SMFRs within the main body of the ICME, and (ii) energization of particles behind the same-type current sheet near the edge of the heliospheric plasma sheet filled with dynamic SMFRs and secondary current sheets between SMFRs produced by magnetic reconnection at the HCS. It is thought that many of the superposed events in Figure 1 belong to the first scenario (see discussion in Khabarova & Zank 2017).

4. The SMFR Acceleration Mechanisms in the Focused Transport Equation

In our focused transport equation for energetic particle acceleration transport and acceleration in an SMFR region (Le Roux et al. 2018), the SMFR acceleration mechanisms discussed above appear with the following expressions:

$$\frac{1}{p}\left\langle \frac{dp}{dt}\right\rangle_{\phi}^{I} = \mu(\nu_{\rm REC}^{I} + \nu_{\rm ACC}^{I}) + \frac{1}{2}(3\mu^2 - 1)\nu_{\rm INC}^{I} + \frac{1}{2}(1-\mu^2)\nu_{\rm COM}^{I}, \quad (1)$$

where p is the magnitude of the particle momentum, t is time, μ is the cosine of the particle pitch angle, $\langle dp/dt\rangle_{\phi}^{I}$ is the particle momentum rate of change averaged over particle gyrophase ϕ, and

$$\begin{aligned}
\nu_{\rm REC}^{I} &= \frac{q}{p}\boldsymbol{E}_{\rm REC}\cdot\boldsymbol{b}_{\circ} = -\frac{q}{p}\delta\boldsymbol{U}_I\times\delta\boldsymbol{B}_I\cdot\boldsymbol{b}_{\circ},\\
\nu_{\rm ACC}^{I} &= -\frac{1}{v}\frac{d\delta\boldsymbol{U}_I}{dt}\cdot\boldsymbol{b},\ \left(\frac{d}{dt} = \frac{\partial}{\partial t} + (\boldsymbol{U}_{\circ}\cdot\nabla)\right)\\
\nu_{\rm INC}^{I} &= -\frac{\delta\boldsymbol{B}_I}{B_{\circ}}\cdot\left(\frac{\delta\boldsymbol{B}_I}{B_{\circ}}\cdot\nabla\right)\delta\boldsymbol{U}_I,\\
\nu_{\rm COM}^{I} &= -(\nabla\cdot\delta\boldsymbol{U}_I). \quad (2)
\end{aligned}$$

In Equation (2), q is the net charge of the particle, v is the particle speed, $\delta\boldsymbol{B}_I$ is the SMFR twist or magnetic island component, and $\boldsymbol{B}_0$ is the SMFR axial or guide field component parallel to a unit vector $\boldsymbol{b}_0$. The SMFR guide field is assumed to be in the direction of the solar wind spiral magnetic field based on the investigation by Hu et al. (2018). We model the magnetic field unit vector $\boldsymbol{b}$ in the limit of a strong guide field $\delta B_I/B_0 \ll 1$ as $\boldsymbol{b} \approx \boldsymbol{b}_0 + \delta\boldsymbol{B}_I/B_0 \approx \boldsymbol{b}_0$. In Equation (2), $\delta\boldsymbol{U}_I$ is the SMFR plasma flow velocity. Assuming that SMFR contraction and merging are occurring mainly in the 2D plane perpendicular to $\boldsymbol{b}_0$ in the presence of a significant guide field (e.g., component reconnection as discussed by Birn et al. 1989 and Dmitruk et al. 2004), we model both $\delta\boldsymbol{U}_I$ and $\delta\boldsymbol{B}_I$ to lie in the 2D plane perpendicular to $\boldsymbol{b}_0$.

In Equation (2), the rate $\nu_{\rm REC}^{I}$ refers to the relative gyrophase-averaged momentum rate of change (sans the μ dependence) due to energetic particle parallel guiding center motion acceleration by the turbulent ideal-MHD reconnection electric field force $\boldsymbol{F}_{\rm REC} = q\boldsymbol{E}_{\rm REC} = -\delta\boldsymbol{U}_I\times\delta\boldsymbol{B}_I$ formed in the reconnection zones of merging magnetic island structures. In other words, we assumed that because we are interested in modeling macro-scale transport and acceleration of energetic particles, the nonideal reconnection electric field on such scales is negligible compared to the ideal reconnection component. The particle simulations of two merging magnetic islands by Du et al. (2018) provide some support for this assumption because they show how the simulation domain-averaged (macro-scale) ratio of the nonideal electric field over the ideal-MHD electric field E_{ni}/E_i decreases when increasing the ion-to-electron mass ratio m_i/m_e to more realistic values, reaching a value of $\sim$0.8 when $m_i/m_e = 400$. Extrapolation of their results would suggest that E_{ni}/E_i will be clearly less than 1 for the correct mass ratio. Because we assume that both $\delta\boldsymbol{U}_I$ and $\delta\boldsymbol{B}_I$ are in the 2D plane perpendicular to $\boldsymbol{b}_0$ (component reconnection), the reconnection electric field $\boldsymbol{E}_{\rm REC}\|\boldsymbol{b}_0$ in Equation (2) (perpendicular to the magnetic island plane). Consider the rate $\nu_{\rm ACC}$ in the second line of Equation (2). This expression determines the relative gyrophase-averaged rate of momentum change in response to parallel guiding center motion acceleration by the parallel noninertial force $\boldsymbol{F}_{\rm ACC} = -m(d\delta\boldsymbol{U}_I/dt\cdot\boldsymbol{b})\boldsymbol{b}$ associated with the field-aligned component of the acceleration of the flow $\delta\boldsymbol{U}_I$ in contracting and merging SMFRs. The rate $\nu_{\rm INC}^{I}$ in Equation (2) determines the relative gyrophase-averaged momentum rate of change for energetic particles experiencing SMFR acceleration from the incompressible parallel component of the SMFR shear-flow tensor in the 2D plane perpendicular to $\boldsymbol{b}_0$, which can be expressed as $\boldsymbol{b}_I\cdot(\boldsymbol{b}_I\cdot\nabla)\delta\boldsymbol{U}_I = \boldsymbol{b}_I\boldsymbol{b}_I\colon\nabla\delta\boldsymbol{U}_I = \sum_i b_{Ii}b_{Ij}\sigma_{ij}^{I} + 1/3(\nabla\cdot\delta\boldsymbol{U}_I)\delta_{ij})$, where $\boldsymbol{b}_I = \delta\boldsymbol{B}_I/B_0$ and the SMFR shear-flow tensor $\sigma_{ij}^{I} = 1/2(\partial\delta U_{Ii}/\partial x_j + \partial\delta U_{Ij}/\partial x_i - 2/3(\nabla\cdot\delta\boldsymbol{U}_I)\delta_{ij})$. Finally, the rate $\nu_{\rm COM}^{I}$ determines the relative gyrophase-averaged momentum rate of change of energetic particles produced by SMFR compression acceleration. The acceleration rates listed in Equation (2) also determine the rate of change of the particle pitch angle in terms of $d\mu/dt$, but there is the additional contribution to $d\mu/dt$ from the magnetic mirroring force energetic particles encounter in SMFRs. This contribution is modeled as $\nu_{\rm REF} = v(\nabla\cdot\boldsymbol{b}_I)$ in the limit of a strong guide magnetic field, and being the only contribution to increase with particle speed, is assumed in our theory for simplicity to be the dominating factor in determining $d\mu/dt$ for energetic particles. As a result of a perturbation analysis of the basic focused transport equation, a modified focused transport equation which distinguishes between mean acceleration rates $\langle\nu_{\rm REC}^{I}\rangle$, $\langle\nu_{\rm ACC}^{I}\rangle$, $\langle\nu_{\rm INC}^{I}\rangle$, $\langle\nu_{\rm COM}^{I}\rangle$ associated with mean SMFR fields and the variance in the acceleration rates $\langle(\delta\nu_{\rm REC}^{I})^2\rangle$, $\langle(\delta\nu_{\rm ACC}^{I})^2\rangle$, $\langle(\delta\nu_{\rm INC}^{I})^2\rangle$, $\langle(\delta\nu_{\rm COM}^{I})^2\rangle$ due to fluctuations in SMFR fields (Le Roux et al. 2015, 2018) was derived.

5. The Telegrapher Parker Transport Equation

To derive a general telegrapher-type Parker transport equation from the modified focused transport equation, we did the following: (i) after assuming that a nearly isotropic particle distribution is the appropriate limit for large-scale transport in the solar wind, we expanded the energetic particle distribution function $f(\boldsymbol{x}, p, \mu, t)$ out to the second moment with respect to μ with the aid of Legendre polynomials and derived the zeroth, first, and second moments of the modified focused transport equation (see also Zank et al. 2014 and Le Roux et al. 2015). (ii) We simplified the first- and second-moment equations to first-order ordinary differential equations (ODEs) for the evolution of $f_1(\boldsymbol{x}, p, t)$ (the first moment of $f(\boldsymbol{x}, p, \mu, t)$) and $f_2(\boldsymbol{x}, p, t)$ (the second moment of $f(\boldsymbol{x}, p, \mu, t)$) with both equations having source terms containing spatial and momentum gradients with respect to $f_0(\boldsymbol{x}, p, t)$ (the zeroth moment of $f(\boldsymbol{x}, p, \mu, t)$). We arrived at the simplified evolution equations for f_1 and f_2 by imposing $f_{1(2)} \ll f_0$, assuming that the pitch-angle scattering time is the shortest timescale in the system and also by retaining $\partial f_{1(2)}/\partial t$ in the first- (second-) moment equations, respectively. (iii) The evolution equations for f_1 and f_2 were solved in terms of gradients f_0, and the solutions were inserted in the zeroth moment equation to arrive at a closed transport equation for $f_0(\boldsymbol{x}, p, t)$, which is the isotropic part of the particle distribution. (iv) The telegrapher transport equation followed by adding the partial time derivative of the transport equation for $f_0(\boldsymbol{x}, p, t)$ to itself and by making a number of simplifying

assumptions to achieve a tractable equation. These are that the initial particle distribution is isotropic ($f_{1(2)}(\boldsymbol{x}, p, 0) = 0$, $\partial f_{1(2)}(\boldsymbol{x}, p, 0)/\partial t = 0$), particle sources are isotropic and slowly varying in time, transport coefficients are slowly varying in time, and particle pitch-angle scattering frequencies are weakly dependent on space, time, and momentum.

The general telegrapher-type Parker transport equation we derived, which describes the evolution of $f_0(\boldsymbol{x}, p, t) = (1/2)\int_{-1}^{1} d\mu f(\boldsymbol{x}, p, \mu, t)$, is given by

$$\begin{aligned}
&\frac{3\kappa_{\parallel}^{I1}}{v^2}\frac{\partial}{\partial t}\left[\frac{\partial f_0}{\partial t} + (\boldsymbol{U}^{\rm coh}\cdot\nabla)f_0\right.\\
&\quad\left. - (\nabla\cdot\boldsymbol{U}^{\rm coh})\frac{p}{3}\frac{\partial f_0}{\partial p} - \frac{1}{p^2}\frac{\partial}{\partial p}\left(p^2 D_{pp}^{\rm Istoch}\frac{\partial f_0}{\partial p}\right)\right]\\
&\quad + \frac{\partial f_0}{\partial t} + \left[\boldsymbol{U}^{\rm coh} - \frac{1}{3p^2}\frac{\partial}{\partial p}(p^3[U_{\rm EA}^{\rm coh} - U^{\rm Istoch}]\boldsymbol{b})\right]\cdot\nabla f_0\\
&\quad - [(\nabla\cdot\boldsymbol{U})^{\rm coh} + \nabla\cdot([U_{\rm EA}^{\rm coh} + U^{\rm Istoch}]\boldsymbol{b})]\frac{p}{3}\frac{\partial f_0}{\partial p}\\
&= \nabla\cdot(\kappa_{\parallel}^{I1}\boldsymbol{b}\boldsymbol{b}\cdot\nabla f_0) + \frac{1}{p^2}\frac{\partial}{\partial p}\left(p^2[D_{pp}^{\rm coh} + D_{pp}^{\rm Istoch}]\frac{\partial f_0}{\partial p}\right)\\
&\quad + \frac{2}{3}pU_{\rm EA}^{\rm coh}(\boldsymbol{b}\cdot\nabla)\frac{\partial f_0}{\partial p}.
\end{aligned} \tag{3}$$

This equation differs from the diffusive Parker transport equation by the presence of additional transport terms in the top line. Besides the well-known telegrapher term (first term in line one of Equation (3) containing the second-order time derivative), there are also additional telegrapher terms involving second- and third-order partial derivatives (the rest of the terms in line one of Equation (3)). The telegrapher Parker transport equation addresses a deficiency in the diffusive Parker transport equation where some particles propagate to larger distances than physically possible by restoring causality. However, the causality in particle transport is only restored for leading-edge particle pulses that are nearly isotropic, that is, for particles that experience significant pitch-angle scattering. It is well known that this kind of telegrapher equation is less accurate when it comes to modeling unscattered particle escape from the acceleration site during early times, resulting in a spatial cutoff in the particle distribution that is too abrupt so that the maximum distance particles reach as a function of time is underestimated (e.g., Effenberger & Litvinenko 2014; Malkov & Sagdeev 2015). In our application of particle acceleration by SMFRs, we model energetic particle acceleration on macro scales inside the SMFR acceleration region where particles are expected to be scattered by low-frequency wave turbulence and by fluctuating magnetic mirroring forces inside these structures to maintain near-isotropic distributions.

In Equation (3), the superscript "coh" refers to a combination of background solar wind quantities and average SMFR quantities, whereas the superscript "Istoch" refers to the variance of fluctuating SMFR quantities only. Thus, $\boldsymbol{U}^{\rm coh}$ represents a net advection effect on energetic particles stemming from the combination of the solar wind velocity with the mean plasma flow velocity in dynamic SMFRs, $U_{\rm EA}^{\rm coh}\boldsymbol{b}$ denotes a net parallel advection effect on energetic particles due to the average parallel component of the electric field and of the acceleration of the plasma flow in the background solar wind and in SMFRs, and $U^{\rm Istoch}\boldsymbol{b}$ refers to the average, field-aligned advection effect produced by the variance in statistical fluctuations in SMFR fields. $\kappa_{\parallel}^{I1}$ denotes the parallel diffusion coefficient as a consequence of particle pitch-angle scattering by random magnetic mirroring forces in SMFRs. The superscript "1" indicates the parallel diffusion coefficient originating from the first anisotropic moment of the underlying focused transport equation to distinguish it from the parallel diffusion coefficient $\kappa_{\parallel}^{I2}$, which follows from the second moment of the focused transport equation ($\kappa_{\parallel}^{I2}$ is not visible in Equation (3), but can be found in Equation (11) for $D_{pp}^{\rm coh}$ further below). Furthermore, there are two categories of second-order Fermi acceleration in Equation (3). $D_{pp}^{\rm coh}$ models second-order Fermi acceleration when particles undergoing pitch-angle scattering respond to the average parallel electric field and acceleration of the plasma flow, and the parallel shear-flow tensor for both the background solar wind and SMFRs, whereas $D_{pp}^{\rm Istoch}$ describes second-order Fermi acceleration when particles experience the variance effects from fluctuations in the same SMFR quantities.

More specifically, in Equation (3),

$$\boldsymbol{U}^{\rm coh} = \boldsymbol{U}_0 + \langle\delta\boldsymbol{U}_I\rangle, \tag{4}$$

where $\boldsymbol{U}_0$ is the background solar wind flow velocity, and $\langle\delta\boldsymbol{U}_I\rangle$ is the mean contraction or merging flow velocity in dynamic SMFRs in the 2D SMFR plane perpendicular to $\boldsymbol{b}_0$. The advection velocity

$$U_{\rm EA}^{\rm coh}\boldsymbol{b} = U_{\rm EA}^{0}\boldsymbol{b}_0 + (U_E^{\rm Icoh}\boldsymbol{b}_0 + U_{\rm A}^{\rm Icoh}\boldsymbol{n}), \tag{5}$$

where

$$\begin{aligned}
U_{\rm EA}^{0} &= \frac{3\kappa_{\parallel}^{I1}}{v}\left(\frac{q\boldsymbol{E}_0}{p} - \frac{1}{v}\frac{d\boldsymbol{U}_0}{dt}\right)\cdot\boldsymbol{b}_0,\\
U_E^{\rm Icoh} &= \frac{3\kappa_{\parallel}^{I1}}{v}\langle\nu_{\rm REC}^{I}\rangle,\\
U_{\rm A}^{\rm Icoh} &= \frac{3\kappa_{\parallel}^{I1}}{v}\langle\nu_{\rm ACC}^{I}\rangle,
\end{aligned} \tag{6}$$

and $U_{\rm EA}^{0}\boldsymbol{b}_0$ expresses the large-scale advection velocity of energetic particles parallel to the background/guide magnetic field direction $\boldsymbol{b}_0$ in response to the combination of a parallel nonideal background electric field component $\boldsymbol{E}_0\cdot\boldsymbol{b}_0$ that becomes significant when charge separation occurs (e.g., at large-scale surfaces such as shocks or current sheets), with the parallel component of the acceleration of the background solar wind flow $d\boldsymbol{U}_0/dt\cdot\boldsymbol{b}_0$. $U_E^{\rm Icoh}\boldsymbol{b}_0$ is the macro-scale energetic particle advection velocity parallel to $\boldsymbol{b}_0$ induced by energetic particles interacting with and getting accelerated by the average ideal-MHD turbulent reconnection electric field parallel to $\boldsymbol{b}_0$. In our quasi-2D SMFR model, the electric field is generated at secondary reconnecting current sheets between merging SMFRs parallel to $\boldsymbol{b}_0$ because of reconnection dynamics in the 2D plane perpendicular to $\boldsymbol{b}_0$ to produce a relative momentum rate of change $\langle\nu_{\rm REC}^{I}\rangle$ as discussed above. Finally, in Equation (6), the velocity $U_{\rm A}^{\rm Icoh}\boldsymbol{n}$ implies the large-scale advection effect on energetic particles produced by the relative momentum rate of

change $\langle \nu_{\rm ACC} \rangle$, when particles interact with the average parallel component of the acceleration of the SMFR flow. The expression for $\langle \nu^I_{\rm ACC} \rangle$ in its final form includes the mean energy density of the SMFR twist or magnetic island component (Le Roux et al. 2018). Based on the assumption of axisymmetric quasi-2D magnetic island turbulence around $\boldsymbol{b}_0$, this advection effect occurs in an arbitrary direction $\boldsymbol{n}$ in the 2D plane perpendicular to $\boldsymbol{b}_0$.

Furthermore, the advection velocity in Equation (3)

$$U^{\rm Istoch}\boldsymbol{b} = \frac{3\kappa^{I1}_{\parallel}}{v}\frac{D^{\rm Istoch}_{pu}}{p}\boldsymbol{n}, \tag{7}$$

where $D^{\rm Istoch}_{p\mu}$ is the pitch-angle averaged Fokker–Planck diffusion coefficient with the expression

$$D^{\rm Istoch}_{p\mu} = \frac{p}{5}(2\langle \delta\nu^I_{\rm COM}\delta\nu^I_{\rm REF}\rangle - \langle \delta\nu^I_{\rm INC}\delta\nu^I_{\rm REF}\rangle)\tau_{\rm dec1}. \tag{8}$$

In Equation (8), $\delta\nu^I_{\rm COM}$ refers to random fluctuations in the SMFR compression acceleration rate of energetic particles induced by fluctuations in the SMFR compression rate, $\delta\nu^I_{\rm INC}$ implies random fluctuations in the SMFR incompressible parallel shear-flow acceleration rate (in the incompressible limit of SMFR acceleration) caused by fluctuations in the SMFR flow velocity and magnetic field, $\delta\nu^I_{\rm REF}$ represents random fluctuations in the energetic particle pitch-angle rate of change due to fluctuations in the magnetic mirroring force in SMFRs, and $\tau_{\rm dec1}$ is the energetic particle decorrelation time (the time energetic particles need to experience decorrelated SMFR fields lying in the 2D plane perpendicular to $\boldsymbol{b}_0$ while propagating through these structures predominantly in the $\boldsymbol{b}_0$ direction). The adiabatic compression term in Equation (3) has the expression

$$(\nabla\cdot\boldsymbol{U})^{\rm coh} = \nabla\cdot\boldsymbol{U}_0 - \langle \nu^I_{\rm COM}\rangle, \tag{9}$$

consisting of the divergence of the background solar wind flow (first term) and the mean SMFR compression rate (second term) that contributes to first-order Fermi SMFR acceleration. Considering second-order Fermi acceleration due to particle pitch-angle scattering coherent or mean fields, the pitch-angle averaged Fokker–Planck momentum diffusion coefficient $D^{\rm coh}_{pp}$ can be decomposed as

$$D^{\rm coh}_{pp} = D^0_{pp} + D^{\rm Icoh}_{pp}, \tag{10}$$

where

$$\begin{aligned}
D^0_{pp} &= p^2\frac{1}{5}(\boldsymbol{b}_0\boldsymbol{b}_0\colon \underline{\sigma}^{\rm sh})^2\frac{\kappa^{I2}_{\parallel}}{v^2} \\
&\quad + p^2\left(\left(\frac{q\boldsymbol{E}_0}{p} - \frac{1}{v}\frac{d\boldsymbol{U}_0}{dt}\right)\cdot\boldsymbol{b}_0\right)^2\frac{\kappa^{I1}_{\parallel}}{v^2}, \\
D^{\rm Icoh}_{pp} &= D^{\rm Icoh}_{\rm COM} = p^2\frac{1}{5}\left(\frac{1}{3}\langle\nu^I_{\rm COM}\rangle\right)^2\frac{\kappa^{I2}_{\parallel}}{v^2} \\
&\quad + D^{\rm Icoh}_{\rm INC} = p^2\frac{1}{5}(\langle\nu^I_{\rm INC}\rangle)^2\frac{\kappa^{I2}_{\parallel}}{v^2} \\
&\quad + D^{\rm Icoh}_{\rm ACC} = p^2(\langle\nu^I_{\rm ACC}\rangle)^2\frac{\kappa^{I1}_{\parallel}}{v^2} \\
&\quad + D^{\rm Icoh}_{\rm REC} = p^2(\langle\nu^I_{\rm REC}\rangle)^2\frac{\kappa^{I1}_{\parallel}}{v^2}.
\end{aligned} \tag{11}$$

In Equations (10) and (11), D^0_{pp} is the momentum diffusion coefficient for second-order Fermi acceleration when energetic particles undergoing pitch-angle scattering interact with the large-scale parallel components of the solar wind shear-flow tensor $\underline{\sigma}^{\rm sh}$, the nonideal background electric field $\boldsymbol{E}_0$ that arises in the solar wind frame when charge separation becomes significant, and the acceleration of the solar wind flow $d\boldsymbol{U}_0/dt$. $D^{\rm Icoh}_{pp}$ models the total second-order Fermi acceleration of scattering particles interacting with mean SMFR fields consisting of the momentum diffusion coefficients $D^I_{\rm COM}$ in response to the average (coherent) SMFR compression acceleration rate $\langle\nu^I_{\rm COM}\rangle$, $D^I_{\rm INC}$ as a consequence of the average incompressible parallel shear-flow acceleration rate $\langle\nu^I_{\rm INC}\rangle$ in SMFRs, $D^I_{\rm ACC}$ associated with the acceleration rate $\langle\nu^I_{\rm ACC}\rangle$ stemming from the mean SMFR parallel flow acceleration, and $D^I_{\rm REC}$ induced by the average parallel reconnection electric field acceleration rate $\langle\nu^I_{\rm REC}\rangle$ in merging SMFRs.

The third and final contribution to second-order Fermi acceleration is supplied by the μ-averaged total momentum diffusion coefficient generated by statistical fluctuations in SMFR fields,

$$\begin{aligned}
D^{\rm Istoch}_{pp} &= D^{\rm Istoch}_{\rm COM} = p^2\left[\frac{2}{15}\langle(\delta\nu^I_{\rm COM})^2\rangle\tau_{\rm dec1}\right. \\
&\quad \left. - \left(\frac{2}{5}\langle\delta\nu^I_{\rm COM}\delta\nu^I_{\rm REF}\rangle\tau_{\rm dec1}\right)^2\frac{\kappa^{I1}_{\parallel}}{v^2}\right] \\
&\quad + D^{\rm Istoch}_{\rm INC} = p^2\left[\frac{1}{5}\langle(\delta\nu^I_{\rm INC})^2\rangle\tau_{\rm dec1}\right. \\
&\quad \left. - \left(\frac{1}{5}\langle\delta\nu^I_{\rm INC}\delta\nu^I_{\rm REF}\rangle\tau_{\rm dec1}\right)^2\frac{\kappa^{I1}_{\parallel}}{v^2}\right] \\
&\quad + D^{\rm Istoch}_{\rm REC} = p^2\frac{1}{3}\langle(\delta\nu^I_{\rm REC})^2\rangle\tau_{\rm dec1} \\
&\quad + D^{\rm Istoch}_{\rm ACC} = p^2\frac{1}{3}\langle(\delta\nu^I_{\rm ACC})^2\rangle\tau_{\rm dec1}.
\end{aligned} \tag{12}$$

In Equation (12), the momentum diffusion coefficients that contribute to second-order Fermi acceleration are $D^{\rm Istoch}_{\rm COM}$, due to the variance in the SMFR compression acceleration rate $\langle(\delta\nu^I_{\rm COM})^2\rangle$, $D^{\rm Istoch}_{\rm INC}$ induced by the variance in the SMFR incompressible parallel shear-flow acceleration rate $\langle(\delta\nu^I_{\rm INC})^2\rangle$, $D^{\rm Istoch}_{\rm REC}$ because of the variance in the parallel reconnection electric field acceleration rate $\langle(\delta\nu^I_{\rm REC})^2\rangle$ generated by the merging of SMFRs, and $D^{\rm Istoch}_{\rm ACC}$ from the variance in the acceleration rate $\langle(\delta\nu^I_{\rm ACC})^2\rangle$ associated with SMFR parallel flow acceleration. The parallel diffusion coefficients $\kappa^{I1(2)}_{\parallel}$ in Equations (11) and (12) have the expressions

$$\begin{aligned}
\kappa^{I1(2)}_{\parallel} &= \frac{1}{3}\frac{v^2}{\langle\nu^{I1(2)}_{\rm sc}\rangle}; \\
\langle\nu^{I1(2)}_{\rm sc}\rangle &= \frac{2}{5(7)}\langle(\delta\nu^I_{\rm REF})^2\rangle\tau_{\rm dec1(2)},
\end{aligned} \tag{13}$$

where $\langle \nu_{\rm sc}^{I1(2)} \rangle$ is the average pitch-angle scattering frequency of energetic particles experiencing nonresonant pitch-angle scattering in response to the variance in random magnetic mirroring forces in SMFRs derived from the first- (second-) moment of the underlying focused transport equation, and $\tau_{\rm dec1(2)}$ is the timescale for propagating particles to see decorrelated SMFR fields specified further below in Section 8.1.

6. Simplified Telegrapher Parker Transport Equation to be Solved Analytically

To enable analytical solutions of the telegrapher Parker transport equation, Equation (3), a number of simplifications was introduced to simplify this equation. It was assumed that energetic particle transport in a solar wind region filled with numerous dynamic SMFRs can be approximated locally as a 1D transport problem in Cartesian geometry in the x direction away from the Sun. For this purpose, we define the background solar wind flow velocity as $\boldsymbol{U}_0 = U_0 \boldsymbol{e}_x$, where $\boldsymbol{e}_x$ is the unit vector pointing in the positive x direction. The background magnetic field $\boldsymbol{B}_0$, which is also assumed to act as the guide field component of SMFRs (Hu et al. 2018), is defined to lie in the ecliptic x–z plane with ψ being the spiral magnetic field angle (the angle between $\boldsymbol{B}_0$ and $\boldsymbol{U}_0$) so that $\boldsymbol{B}_0 = B_0(\cos\psi \boldsymbol{e}_x + \sin\psi \boldsymbol{e}_z)$. It is assumed that the average plasma flow velocity in numerous dynamic SMFRs $\langle \delta \boldsymbol{U}_I \rangle = 0$. The energy density of the magnetic island (twist) component $\delta \boldsymbol{B}_I$ of SMFRs is assumed to be axisymmetrically distributed around $\boldsymbol{B}_0$, on average. Thus, in the x direction, the SMFR advection terms $U_{\rm A}^{\rm Icoh}\boldsymbol{n}$, $U^{\rm Istoch}\boldsymbol{n}$ produce a zero net advection effect on energetic particles and can be ignored. The remaining transport coefficients in Equation (3), namely $\boldsymbol{U}^{\rm coh} \approx \boldsymbol{U}_0$, $U_{\rm EA}^{\rm coh}\boldsymbol{b} \approx (U_{\rm EA}^0 + U_{\rm EA}^{\rm Icoh})\boldsymbol{b}_0$, $\langle \nu_{\rm COM}^I \rangle$, $\kappa_{\parallel}^{I1,2}$, $D_{pp}^{\rm coh}/p^2$, and $D_{pp}^{\rm Istoch}/p^2$, are specified as constants to facilitate analytical solutions.

For analytical simplicity, only the telegrapher term containing $\partial^2 f_0/\partial t^2$ (the first term in the first line of Equation (3)) is retained. This can be partially justified because, based on dimensional analysis of the telegrapher terms and the specification of typical SMFR parameters at 1 au in those terms, we find that the third and for the most part the fourth (last) telegrapher terms are small relative to the first one. The fourth telegrapher term is negligible for all second-order Fermi acceleration mechanisms generated by statistical fluctuations in SMFR fields except for the one associated with the variance in the parallel reconnection electric field (see Equations (12) and (32)). However, the latter mechanism is not considered for modeling acceleration because the analytical solutions only hold for speed-independent values for D_{pp}/p^2. The second telegrapher term, on the other hand, is of the same order as the first one. Thus, ignoring the effect of solar wind advection in the telegrapher terms is a limitation in our analytical solution. As we argue below in Section 7.1, retaining the second telegrapher term in the analytical solution should result in an improvement in the causality condition for particle propagation. Because the improvement is insignificant for particles with $v \gg U_0$, we conclude that the second telegrapher term can be ignored for energetic particles, which is the main focus of this paper.

After implementation of these simplifications, the transport equation that needs to be solved is

$$\tau_{\rm sc}^{I1}\frac{\partial^2 f_0}{\partial t^2} + \frac{\partial f_0}{\partial t} + U_0^I\frac{\partial f_0}{\partial x} + \frac{1}{3}\langle \nu_{\rm COM}^I \rangle p\frac{\partial f_0}{\partial p} = \kappa_{xx}^{I1}\frac{\partial^2 f_0}{\partial x^2} + \frac{1}{p^2}\frac{\partial}{\partial p}\left(p^2 D_{pp}^I \frac{\partial f_0}{\partial p}\right) + \frac{2}{3}U_E^I\frac{\partial}{\partial x}\left(p\frac{\partial f_0}{\partial p}\right) - \frac{f_0}{\tau_{\rm esc}} + Q, \quad (14)$$

where Q is a particle source for injection into the SMFR region and $-f_0/\tau_{\rm esc}$ is a loss term that was added to model particle escape from the SMFR region on a characteristic timescale $\tau_{\rm esc}$ following the example of Zhao et al. (2018) and Adhikari et al. (2019). In Equation (14), the effective advection speed U_0^I is expressed as

$$U_0^I = U_0 - U_E^I,$$

where

$$U_E^I = \frac{3\kappa_{\parallel}^{I1}}{v}\langle \nu_{\rm REC}^I \rangle \cos\psi. \quad (15)$$

In the inner heliosphere, the diffusion coefficient in the x direction, $\kappa_0^I = \kappa_{xx}^{I1}$, is specified as

$$\kappa_0^I = \kappa_{\parallel}^{I1}\cos^2\psi, \quad (16)$$

implying that the contribution of perpendicular diffusion is negligible. The total momentum diffusion coefficient for second-order Fermi acceleration by SMFRs

$$D_{pp}^I = p^2 D_0^I = D_{pp}^{\rm Icoh} + D_{pp}^{\rm Istoch}, \quad (17)$$

where $D_{pp}^{\rm Icoh}$ is expressed by Equation (11) and $D_{pp}^{\rm Istoch}$ by Equation (12).

7. Analytical Time-dependent Solutions

7.1. Time-dependent Solution of the Telegrapher Parker Transport Equation

For a steady-state point source Q of energetic particles continually injected at a fixed rate dN_0/dt at position $x = x_0$ and at momentum $p = p_0$ with the expression

$$Q(x, p) = \left(\frac{dN_0/dt}{4\pi p_0^2}\right)\delta(x - x_0)\delta(p - p_0), \quad (18)$$

the solution of Equation (14) is

$$f_0(x,p,t) = \frac{1}{2\pi}\left(\frac{dN_0/dt}{4\pi p_0^3}\right)\frac{1}{\sqrt{\overline{D}_0^I \tau_{\rm sc}^{I1}}} \times \exp\left(\frac{1}{2}\left[\frac{U_0^I + qU_E^I/3}{\kappa_0^I}\right](x-x_0)\right)\left(\frac{p}{p_0}\right)^{-q/2} \times \int_0^t d\tau \exp\left(-\frac{1}{2}\frac{\tau}{\tau_{\rm sc}^{I1}}\right)\frac{\cosh\left(c\sqrt{v_c^2\tau^2 - d^2}\right)}{\sqrt{v_c^2\tau^2 - d^2}} \times H(p-p_0)H(\tau)H(v_c\tau - d)H\left(1 - \frac{1}{9}\frac{(U_E^I)^2}{\kappa_0^I D_0^I}\right), \quad (19)$$

where

$$\tau = t - t_0,$$
$$v_c = \sqrt{\frac{\kappa_0^{I1}}{\tau_{\rm sc}^{I1}}} = \frac{v}{\sqrt{3}},$$
$$\overline{D}_0^I = D_0^I\left(1 - \frac{1}{9}\frac{(U_E^I)^2}{\kappa_0^I D_0^I}\right),$$
$$q = \left(3 - \frac{1}{3}\frac{\langle \nu_{\rm COM}\rangle - U_0^I U_E^I/\kappa_0^I}{D_0^I}\right)\Bigg/\left(1 - \frac{1}{9}\frac{(U_E^I)^2}{\kappa_0^I D_0^I}\right),$$
$$c = \sqrt{\frac{\tau_{\rm sc}^{I1}}{\kappa_0^I}\left(\frac{1}{2\tau_{\rm sc}^I}\right)^2 - \left(\frac{1}{2}\frac{U_0^I}{\kappa_0^{I1}}\right)^2 - \frac{1}{\kappa_0^{I1}\tau_{\rm esc}} - \frac{\overline{D}_0^I}{\kappa_0^I}\left(\frac{q}{2}\right)^2},$$
$$d = \sqrt{(x-x_0)^2 + \frac{\kappa_0^I}{\overline{D}_0^I}\left[\ln\left(\frac{p}{p_0}\right) - \frac{1}{3}\left(\frac{U_E^I}{\kappa_0^I}\right)(x-x_0)\right]^2}. \quad (20)$$

The expression $v_c = \sqrt{\kappa_0^I/\tau_{\rm sc}^{I1}} = v/\sqrt{3}$ indicates the telegrapher speed (the speed at which the leading pulse of scattered particles is modeled to travel in the limit of a nearly isotropic particle distribution), whereas the Heaviside step function $H(v_c\tau - d)$ indicates the causality condition which constrains how far the leading pulse of scattered particles with a characteristic speed $v_c = v/\sqrt{3}$ can travel. Note that the causality condition is not entirely in the fixed frame of reference because the particle speed v in v_c is valid in the solar wind flow frame whereas τ and d are fixed-frame quantities. We speculate that if we retain the second telegrapher term associated with the solar wind advection of energetic particles (the second term in the first line of Equation (3)) in the analytical solution, this defect in the causality condition will be corrected so that it reads $(U_0 + v_c)\tau + d > 0$, where $U_0 + v_c$ is the particle pulse speed in the fixed frame. However, for fast particles with $v \gg U_0$, the main focus of this paper, this correction is negligible and ignoring the second telegrapher term can be justified.

To further investigate the causality condition, we put $v_c\tau - d = 0$ and solving for $\ln(p/p_0)$ to get the expression

$$\ln\left(\frac{p}{p_0}\right) = \frac{1}{3}\frac{U_E^I}{\kappa_0^I}(x - x_0) \pm \frac{1}{\kappa_0^I}\sqrt{D_0^I\kappa_0^I\left(1 - \frac{1}{9}\frac{(U_E^I)^2}{\kappa_0^I D_0^I}\right)(v_c^2\tau^2 - (x-x_0)^2)}. \quad (21)$$

For $\ln(p/p_0)$ to be real requires that both $1 - (U_E^I)^2/(9D_0^I\kappa_0^I) > 0$ and $v_c^2\tau^2 - (x-x_0)^2 > 0$. If $1 - (U_E^I)^2/(9D_0^I\kappa_0^I) < 0$, the requirement is that $v_c^2\tau^2 - (x-x_0)^2 < 0$ for $\ln(p/p_0)$ to be real. However, $v_c^2\tau^2 - (x-x_0)^2 < 0$ implies that for any given time interval τ, particles did not reach the arbitrary observation point x so that the solution is $f_0(x,t) = 0$. This zero solution arises when $D_0^I < (U_E^I)^2/(9\kappa_0^I)$, that is, when second-order Fermi acceleration by SMFRs is negligible compared to acceleration by the mean parallel reconnecting electric field in merging SMFRs through the mixed-derivative acceleration term $(2/3)pU_E^I(\partial^2 f_0/\partial x\partial p)$ in Equation (14). Within the framework of the time-dependent telegrapher solution, it is thus necessary to constrain the strength of particle acceleration by the mean parallel reconnection electric field of SMFRs sufficiently relative to second-order Fermi acceleration by SMFRs. Furthermore, a solution of SMFR acceleration involving the mixed-derivative term is not viable without second-order Fermi acceleration, thus emphasizing the need to include the latter in SMFR acceleration studies. Solution (19) is our most complete solution to date because it combines first-order Fermi SMFR acceleration, second-order Fermi SMFR acceleration, and SMFR acceleration by the mixed-derivative acceleration term for the mean parallel reconnection electric field. The second-order Fermi acceleration coefficient D_0^I includes contributions from both D_{pp}^{Ioch} and $D_{pp}^{\rm Istoch}$.

7.2. Time-dependent Solution of Diffusive Parker Transport Equation

We also found an analytical solution for the time-dependent diffusion–advection Parker transport equation (Equation (14) without the telegrapher term (first term)). This solution, which can be shown to be consistent with taking a late-time asymptotic of solution (19), is given by

$$f_0(x,p,t) = \frac{1}{4\pi}\left(\frac{dN_0/dt}{4\pi p_0^3}\right)\frac{1}{\sqrt{\overline{D}_0^I\kappa_0^I}} \times \exp\left(\frac{1}{2}\left[\frac{U_0^I + qU_E^I/3}{\kappa_0^I}\right](x-x_0)\right)\left(\frac{p}{p_0}\right)^{-q/2} \times \int_0^t d\tau\frac{1}{\tau}\exp\left(-\frac{\alpha}{\tau}\right)\exp(-\beta\tau), \quad (22)$$

where

$$\alpha = \frac{1}{4\kappa_0^I}\left((x-x_0)^2 + \frac{\kappa_0^I}{\overline{D}_0^I} \times \left[\ln\left(\frac{p}{p_0}\right) - \frac{1}{3}\left(\frac{U_E^I}{\kappa_0^I}\right)(x-x_0)\right]^2\right) = \frac{d^2}{4\kappa_0^I},$$
$$\beta = \left(\frac{1}{2}\frac{U_0^I}{\kappa_0^I}\right)^2\kappa_0^I + \frac{1}{\tau_{\rm esc}} + \left(\frac{q}{2}\right)^2\overline{D}_0^I, \quad (23)$$

where the expression for α is related to the expression for d in Equation (20), the expression for β is a simplified version of expression c in Equation (20) (without the telegrapher effect), and the rest of the parameters were already defined in Equation (20).

8. Steady-state Limit of the Time-dependent Solution of the Diffusive Parker Transport Equation

By letting the time interval $\tau \to \infty$ in solution (22), one finds the steady-state limit of the time-dependent solution of the diffusive Parker transport equation. The solution is

$$f_0(x,p) = \frac{1}{2\pi}\left(\frac{dN_0/dt}{4\pi p_0^3}\right)\frac{1}{\sqrt{\overline{D}_0^I\kappa_0^I}} \times \exp\left(\frac{1}{2}\left[\frac{U_0^I + qU_E^I/3}{\kappa_0^I}\right](x-x_0)\right)\left(\frac{p}{p_0}\right)^{-q/2} \times K_0(2\sqrt{\alpha\beta}), \quad (24)$$

where K_0 is the modified Bessel function of the second kind, and the rest of the parameters were defined in Equations (20) and (23).

Inspection of the solution reveals the basic characteristics of observations of energetic particle acceleration and transport through a dynamic SMFR region in the solar wind, namely, energetic particle distribution spatial peak formation and spectral hardening as discussed above. By taking the limit $\ln^2(p/p_0) \gg (x-x_0)^2$ in the parameter α in $K_0(2\sqrt{\alpha\beta})$, one finds that

$$f_0(x,p) \propto e^{\frac{1}{2}\frac{U_0}{\kappa_0^I}(x-x_0)} \times \left(\frac{p}{p_0}\right)^{-\frac{1}{2}[q+|q|\sqrt{1+(2/q)^2\tau_{D_0^I}[1/\tau_{\kappa_0^I}+1/\tau_{\rm esc}]}]}. \quad (25)$$

If instead one takes the opposite limit $(x-x_0)^2 \gg \ln^2(p/p_0)$ in the parameter α in $K_0(2\sqrt{\alpha\beta})$,

$$f_0(x,p) \propto e^{-\frac{1}{2}[|U_0(x-x_0)|\sqrt{1+4\tau_{\kappa_0^I}[(q/2)^2/\tau_{D_0^I}+1/\tau_{\rm esc}]}-U_0(x-x_0)]/\kappa_0^I} \times (p/p_0)^{-q/2}. \quad (26)$$

In Equations (25) and (26), we introduced the characteristic timescales $\tau_{D_0^I} = 1/D_0^I$ (acceleration timescale for second-order Fermi acceleration) and $\tau_{\kappa_0^I} = \kappa_0^I/U_0^2$ (diffusion timescale). As before, $\tau_{\rm esc}$ is the timescale for particle escape from the SMFR acceleration region. These solution limit expressions were simplified for easier interpretation by putting $U_E^I = 0$. Thus, we removed the effect of the mixed-derivative reconnection electric field transport term in Equation (14) which counteracts spatial peak formation in the accelerated particle distributions in SMFR regions contrary to observations (Zank et al. 2014). Both solution limits (25) and (26) indicate that, because energetic particle diffusive transport occurs against the solar wind flow upstream of the particle injection point at x_0 ($x < x_0$), the particle distribution decays exponentially with increasing upstream distance from x_0 (no spatial peak in the particle distribution). Because diffusive transport unfolds in the direction of the solar wind flow downstream of the injection point ($x > x_0$) during acceleration, the particle distribution increases exponentially with increasing distance downstream when sufficiently close to the injection point because then limit (25) applies. However, sufficiently far downstream of the injection point, the particle distribution at lower energies decays first with increasing distance because then limit (26) is applicable. The decay at higher energies occurs progressively farther downstream of the particle source when limit (26) becomes applicable at those distances. Thus, peaks form in the accelerated downstream distribution that shifts increasingly to larger distances downstream with increasing particle energy.

Consider the particle spectra. Close to the injection point, the particle spectra form power laws steeper than $f_0(p) \propto (p/p_0)^{-q/2}$ at most energies above the injection energy ($p > p_0$) because limit (25) is valid. With increasing distance from the injection point, expression (25) holds progressively at increasingly high particle energies only while at lower energies, limit (26) applies where the spectrum approaches the harder power law $f_0(p) \propto (p/p_0)^{-q/2}$ for a growing energy interval. Thus, with increasing distance from the injection point, the accelerated particle spectrum becomes increasingly hard on average while assuming a more exponential character as it bends over more strongly at lower energies. Inspection of limit (25) also reveals that more efficient particle escape results in a steeper spectrum (Zhao et al. 2018), and a larger spatial diffusion coefficient produces a harder spectrum as particles sample more SMFRs in a given time interval.

8.1. Limits of the Steady-state Solution

8.1.1. First-order Fermi Acceleration by SMFRs (Compression Acceleration)

One can find the correct steady-state limit for energetic particle acceleration when first-order Fermi acceleration (SMFR mean compression acceleration) dominates if one lets $U_E^I \to 0$ and $D_0^I \to 0$ so that $(\langle\nu_{\rm COM}^I/3) \gg D_0^I$ in the general

steady-state solution (24). It then follows that

$$f_0(x,p) = \left(\frac{dN_0/dt}{4\pi p_0^3}\right)\frac{1}{\langle\nu^I_{\rm COM}\rangle/3} \times \exp\left(\frac{1}{2}\frac{U_0}{\kappa^I_0}(x-x_0)\right)\left(\frac{p}{p_0}\right)^{-\frac{(U_0/(2\kappa^I_0))^2\kappa^I_0+1/\tau_{\rm esc}}{\langle\nu^I_{\rm COM}\rangle/3}} \times \frac{\exp\left(-\frac{(x-x_0)^2}{4\kappa^I_0/(\langle\nu^I_{\rm COM}\rangle/3)}\frac{1}{\ln(p/p_0)}\right)}{\sqrt{4\pi\kappa^I_0/(\langle\nu^I_{\rm COM}\rangle/3)\ln(p/p_0)}}H(p-p_0). \quad (27)$$

At the particle source position $x = x_0$, the accelerated particle spectrum is $f_0(p) \propto (p/p_0)^{-3\tau^I_{\rm COM}(1/4\tau_{\kappa^I_0}+1/\tau_{\rm esc})}$, where $\tau^I_{\rm COM} = 1/\langle\nu^I_{\rm COM}\rangle$ is the timescale for the SMFR mean compression acceleration and $\tau^I_{\kappa^I_0} = \kappa^I_0/U_0^2$ is the timescale for effective diffusion relative to the solar wind flow with speed U_0. Consistent with the general solution (24), the expression for the power-law index suggests that (i) the more effective energetic particle diffusion becomes in the region of SMFRs (increase in $\tau_{\kappa^I_0}$), the harder the accelerated spectrum becomes. Thus, SMFR compression acceleration becomes more efficient if energetic particles cross more SMFRs in a given time period. (ii) The accelerated spectrum becomes harder when the mean SMFR compression rate is enhanced (reduction of $\tau^I_{\rm COM}$). (iii) More efficient energetic particle escape from the SMFR region (smaller value for $\tau_{\rm esc}$) results in a steeper accelerated particle spectrum. In the limit $\tau^I_{\rm COM} \ll \tau_{\kappa^I_0}$ and $\tau^I_{\rm COM} \ll \tau_{\rm esc}$, the accelerated spectrum converges to $f_0(x_0,p) \propto p^0$ so that asymptotically, we arrive at a flat accelerated spectrum for test particles near the particle injection point. There are further qualitative similarities to the general solution. From inspection of the two exponential functions in Equation (27), it is clear that downstream of the injection point $x > x_0$, the accelerated particles will form a spatial peak in the SMFR region with the second exponential providing the spatial decay of the distribution. The second exponential function also suggests that with increasing distance from the injection location, the accelerated particle spectrum will be more likely to bend over at lower energies. Different from the general solution, however, the downstream spectrum cuts off at the injection momentum $p = p_0$.

8.1.2. Second-order Fermi Acceleration by SMFRs

By taking the limits $U^I_E \to 0$, and $\langle\nu^I_{\rm COM}\rangle \to 0$ in Equation (24), one recovers the correct steady-state solution for second-order Fermi acceleration by SMFRs given by

$$f_0(x,p) = \frac{1}{2\pi}\left(\frac{dN_0/dt}{4\pi p_0^3}\right)\frac{1}{\sqrt{D^I_0\kappa^I_0}} \times \exp\left(\frac{1}{2}\frac{U_0}{\kappa^I_0}(x-x_0)\right)\left(\frac{p}{p_0}\right)^{-3/2} \times K_0(2\sqrt{\alpha\beta})H(p-p_0), \quad (28)$$

where

$$\alpha = \frac{1}{4\kappa^I_0}\left[(x-x_0)^2 + \frac{\kappa^I_0}{D^I_0}\ln^2\left(\frac{p}{p_0}\right)\right],$$
$$\beta = \left(\frac{1}{2}\frac{U_0}{\kappa^I_0}\right)^2\kappa^I_0 + \frac{1}{\tau_{\rm esc}} + \frac{9}{4}D^I_0. \quad (29)$$

Upon assuming strong second-order Fermi acceleration ($D^I_0 \gg U_0^2/\kappa^I_0$, and $D^I_0 \gg 1/\tau_{\rm esc}$) at $x = x_0$, we find that the accelerated energetic particle spectrum converges to $f_0(x_0,p) \propto p^{-3}$, which is the hardest spectrum possible in the test particle limit at the particle injection location. The basic features of the general solution as deduced from limits (25) and (26), namely, spatial peak formation and spectral hardening in the accelerated energetic particle distribution in the SMFR region downstream of the injection point, and other aspects discussed as well, are valid when only second-order Fermi acceleration occurs.

8.1.3. Acceleration by the Mean Parallel Reconnection Electric Field (Mixed-derivative Transport Term)

By ignoring the first- and second-order Fermi SMFR acceleration terms ($\langle\nu^I_{\rm COM}\rangle \to 0$ and $D^I_0 \to 0$ in Equation (24)), particle acceleration is determined by the mixed-derivative term $(2/3)pU^I_E\partial^2 f_0/\partial x\partial p$ describing a certain aspect of energetic particle acceleration by the average parallel reconnection electric field in merging SMFRs. Upon assuming $U^I_E < 0$, we find that the real part of the solution yields

$$f_0(x,p) = \left(\frac{dN_0/dt}{4\pi p_0^3}\right)\frac{3}{4}\frac{1}{|U^I_E|} \times \left(\frac{p}{p_0}\right)^{-\frac{3}{2}\frac{U^I_0}{|U^I_E|}}[J_0(3\sqrt{\alpha\beta_1})H(\beta_1)H(x_0-x) + J_0(3\sqrt{\alpha\beta_2})H(x-x_0)]H(p-p_0), \quad (30)$$

where

$$\alpha = \frac{\kappa^I_0/(U^I_E)^2}{\tau_{\rm esc}}\ln\left(\frac{p}{p_0}\right),$$
$$\beta_1 = \ln\left(\frac{p}{p_0}\right) - \frac{2}{3}\frac{|U^I_E|}{\kappa^I_0}(x_0-x),$$
$$\beta_2 = \ln\left(\frac{p}{p_0}\right) + \frac{2}{3}\frac{|U^I_E|}{\kappa^I_0}(x-x_0), \quad (31)$$

and J_0 is the Bessel function of the first kind. This solution is a factor of 2 larger than the correct solution. By dividing the solution by a factor of 2, and by taking the limit of no particle escape $\tau_{\rm esc} \to \infty$, $J_0 \to 1$ so that we reproduce the steady-state solution published first in Zank et al. (2014). Upon taking the limit of strong acceleration by the parallel electric field $|U^I_E| \gg U_0$ so that $U^I_0 \approx |U^I_E|$ and $J_0 \approx 1$, we find that the

accelerated spectrum converges to $f_0(x_0, p) \propto p^{-3/2}$ (Zank et al. 2014). Note that without particle escape, the distribution function forms a plateau (Zank et al. 2014). Inclusion of particle escape results in a distribution function that decays on large scales with increasing distance $x - x_0$ downstream of the injection point when $\ln(p/p_0) < (2/3)|U_E^I|(x - x_0)/\kappa_0^I$ in the β_2 parameter in the argument of $J_0(3\sqrt{\alpha\beta_2})$. This decay can be explicitly expressed far downstream of the injection point because then $(x - x_0)/(|U_E^I|\tau_{\rm esc}) \gg 1$, so that $J_0(3\sqrt{\alpha\beta_2}) \approx \sqrt{2/(\pi 3\sqrt{\alpha\beta_2})}\cos(3\sqrt{\alpha\beta_2})$. Thus, different from the acceleration mechanisms discussed above, there is no large-scale peak formation in the accelerated particle distribution downstream of the injection location.

9. Modeling SMFR Energetic Particle Acceleration Events at Earth Orbit

In this section, we apply our analytical solutions to model observed energetic particle flux amplification inside solar wind regions filled with SMFRs generated near reconnecting large-scale current sheets at 1 au. We want to investigate whether such flux amplification can potentially be reproduced by specifying reasonable SMFR parameters in our expressions for the SMFR acceleration mechanisms, because up to now reproduction of observed flux amplification was achieved without linking the strength of SMFR acceleration mechanisms to SMFR parameters (Zhao et al. 2018; Adhikari et al. 2019). Furthermore, we want to analyze the potential of second-order Fermi acceleration by SMFRs to reproduce these observations, because the Zhao et al. (2018) and Adhikari et al. (2019) modeling efforts considered the interplay between first-order Fermi acceleration by SMFRs and acceleration by the mean parallel reconnection electric field of merging SMFRs through the mixed-derivative acceleration term in Equation (14). For this purpose, we are guided by the observed energetic ion flux enhancements in Figures 10 and 11 in Khabarova & Zank (2017), which are merged in Figure 1 in this paper.

9.1. Second-order Fermi Acceleration due to Fluctuations in SMFR Fields

In this section, we investigate the acceleration of energetic particles by SMFRs in the limit of second-order Fermi acceleration generated by statistical fluctuations in SMFR properties using the steady-state solution given by Equations (28) and (29). Thus, we ignore all SMFR acceleration mechanisms involving mean SMFR properties by setting $\langle \nu_{\rm COM}\rangle = 0$, $U_E^I = 0$, and $D_{pp}^{\rm Icoh} = 0$, so that $D_{pp}^I = D_{pp}^{\rm Istoch}$ (see Equation (17)). The expressions for $D_{pp}^{\rm Istoch}$ used in the modeling followed from the manipulation of the related basic expressions in Equation (12) for the purpose of expressing them in terms of familiar SMFR turbulence observational parameters. Assumptions used in this process are that dynamic SMFRs behave like quasi-2D MHD turbulence in the strong guide field limit that are statistically randomly distributed in the 2D plane perpendicular to the guide field. Details can be found in Appendix A of Le Roux et al. (2018). The acceleration expressions in the case of ion transport are

$$
\begin{aligned}
D_0^I &= D_{pp}^{\rm Istoch}/p^2 \\
&= D_{\rm COM}^{\rm Istoch}/p^2 = \frac{1}{15}\left[r_{\rm A}^I - \frac{1}{4}(\sigma_c^I)^2(r_{\rm A}^I+1)^2\right] \\
&\quad\times \frac{\langle \delta B_I^2\rangle}{B_0^2}\left(\frac{V_{\rm A0}}{L_I}\right)^2\tau_{\rm dec1} \\
&\quad + D_{\rm INC}^{\rm Istoch}/p^2 = \frac{1}{5}\left[r_{\rm A}^I + \frac{1}{4}(\sigma_c^I)^2(r_{\rm A}^I+1)^2\right] \\
&\quad\times \left(\frac{\langle \delta B_I^2\rangle}{B_0^2}\right)^3\left(\frac{V_{\rm A0}}{L_I}\right)^2\tau_{\rm dec1} \\
&\quad + D_{\rm REC}^{\rm Istoch}/p^2 = \frac{1}{3}\left[r_{\rm A}^I - \frac{1}{4}(\sigma_c^I)^2(r_{\rm A}^I+1)^2\right] \\
&\quad\times \left(\frac{\langle \delta B_I^2\rangle}{B_0^2}\right)^2\left(\frac{V_{\rm A0}}{\nu}\right)^2\left(\frac{V_{\rm A0}}{d_i}\right)^2\tau_{\rm dec1}, \\
&\quad + D_{\rm ACC}^{\rm Istoch}/p^2 = \frac{1}{6}r_{\rm A}^I\frac{\langle \delta B_I^2\rangle}{B_0^2}\left(\frac{U_0}{\nu}\right)^2\left(\frac{V_{\rm A0}}{L_{Ix}}\right)^2\tau_{\rm dec1}, \qquad (32)
\end{aligned}
$$

where $r_{\rm A}^I$ is the Alfvén ratio for SMFRs (ratio of the mean SMFR kinetic energy over magnetic energy in the 2D plane perpendicular to the guide/background magnetic field), σ_c^I is the SMFR normalized cross-helicity (for definition, see Le Roux et al. 2018), $\langle \delta B_I^2\rangle/B_0^2$ is the ratio of the mean twist (magnetic) island component energy density over the axial (guide) magnetic field energy density of SMFRs, $V_{\rm A0}$ is the Alfvén speed for the guide/background magnetic field, d_i is the proton inertial scale, $\tau_{\rm dec1}$ is the timescale needed for propagating particles to see decorrelated SMFR fields, and L_{Ix} is the value of the SMFR cross section projected in the solar wind flow direction. In expression (13) for $\kappa_\parallel^{I1(2)}$, $\tau_{\rm dec1(2)}$ is modeled by assuming that energetic particles encounter decorrelated SMFR fields on a shorter timescale in the guide field direction as compared to that in the island magnetic field direction perpendicular to the guide field (the assumption is that particle propagation is most efficient along the magnetic field, which is approximately in the guide field direction in the strong guide field limit). This requires deciding on the parallel particle propagation model inside SMFRs. We assume that energetic particles encounter sufficiently strong fluctuating magnetic mirroring forces inside SMFRs so that parallel propagation inside SMFRs is diffusive. This is expected to be the case when smaller-scale flux rope structures with sizes more comparable to the particle gyroradius exist inside SMFRs as the result of a forward quasi-2D turbulence cascade, acting as scattering centers for energetic particles. Thus, we operate in the regime of a disturbed orbit nonlinear theory for parallel diffusion that yielded a nonlinear equation for parallel diffusion with the solution

$$
\kappa_\parallel^{I1(2)} = \frac{100(136)}{9\pi}\frac{(r_{\rm A}^I)^{1/2}}{(\langle \delta B_I^2\rangle/B_0^2)^{3/2}}\left(\frac{L_I}{L_{I\parallel}}\right)^3 L_{I\parallel}V_{\rm A0}, \qquad (33)
$$

where L_I is the cross section of SMFRs and $L_{I\parallel}$ is the dimension of SMFRs in the guide field direction (for more details, see Le Roux et al. 2015, 2016, 2018). Consequently, the particle

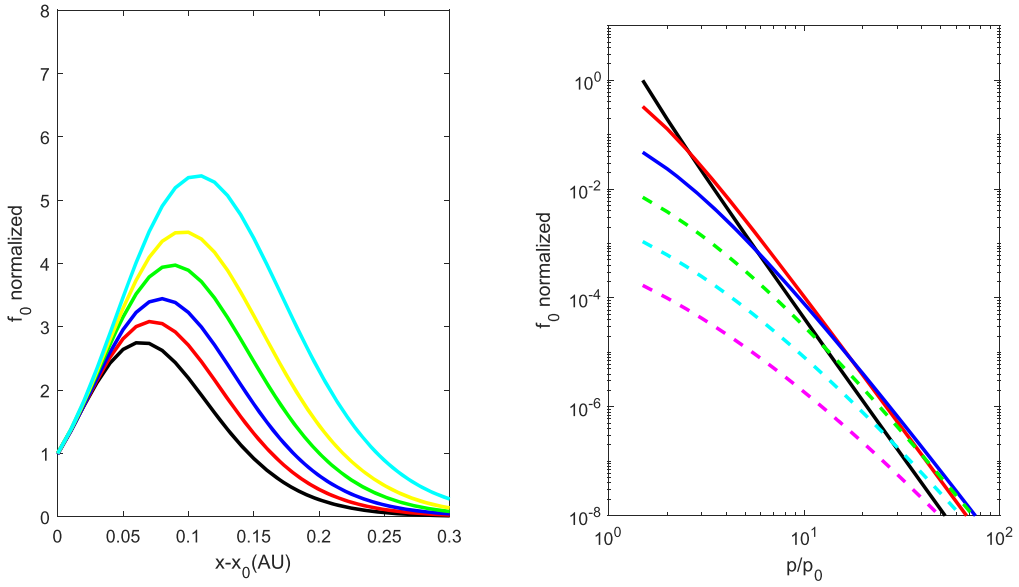

Figure 2. The 1D steady-state analytical solution (Equation (28)) for energetic proton second-order Fermi acceleration by SMFRs near 1 au combining acceleration due to the variance in the SMFR compression and in the incompressible parallel shear flow. Left panel: the direction-averaged proton distribution function $f_0(x, p)$ as a function of relative distance $x - x_0$ in astronomical units (au; distance relative to the particle injection position x_0 in the downstream direction (in the direction of the solar wind flow)) for particle energies 144 keV (black), 256 keV (red), 0.44 MeV (blue), 0.81 MeV (green), 1.44 MeV (yellow), and 3.31 MeV (cyan). Each curve was normalized to a value of 1 at the injection position ($x - x_0 = 0$ au). Thus, values of $f_0 > 1$ indicate amplification of f_0 whereas values of $f_0 < 1$ represent a decrease in f_0 relative to the injection location. Right panel: $f_0(x, p)$ as a function of particle momentum p in the solar wind frame normalized to p_0 (the injection momentum). The spectra are displayed for the following values of $x - x_0$: 0 au (solid black), 0.05 au (solid red), 0.1 au (solid blue), 0.15 au (dashed green), 0.2 au (dashed cyan), and 0.25 au (dashed magenta). The curves were multiplied with the same factor so that the curve at the injection position (black curve) has a value of 1 at the minimum momentum $p/p_0 = 1.5$. At $p/p_0 = 1$, the proton kinetic energy $T \approx 1$ keV while at the maximum momentum, $p/p_0 = 100$, $T \approx 10$ MeV.

decorrelation time $\tau_{\rm dec1(2)}$ can be expressed as

$$\tau_{\rm dec1(2)} = \left[\frac{3\pi}{20(28)}\frac{L_{I\parallel}}{L_I}\left(\frac{\langle \delta B_I^2\rangle / B_0^2}{r_{\rm A}^I}\right)^{1/2}\right]\frac{L_{I\parallel}}{V_{\rm A0}}. \quad (34)$$

With the aid of Equation (33), the particle scattering time can be estimated using the expression

$$\tau_{\rm sc}^{I1(2)} = 1/\nu_{\rm sc}^{I1(2)} = \frac{3}{v^2}\kappa_{\parallel}^{I1(2)}. \quad (35)$$

Remarkably, this model for parallel diffusion is independent of particle speed, indicative of temporary particle trapping inside SMFRs due to magnetic mirroring combined with a small separation distance between neighboring SMFRs so that the crossing time between neighboring SMFRs is negligible compared to the trapping time. The theory for parallel diffusion justifies specifying a constant diffusion coefficient, thus facilitating our analytical solutions presented above.

9.1.1. Steady-state Solutions

We present analytical steady-state results in Figure 2 for second-order Fermi acceleration in response to the variance in SMFR fields combining the effects of $D_{\rm COM}^{\rm Istoch}$ and $D_{\rm INC}^{\rm Istoch}$. We do not include the acceleration effect of $D_{\rm ACC}^{\rm Istoch}$ or of $D_{\rm REC}^{\rm Istoch}$ because both these mechanisms contribute terms with a v^{-2} dependence in the second-order Fermi parameter D_0^I in solution (28), which is only valid for a constant D_0^I value. In Figure 2 (left panel), we display the modeled spatial peak formation in the direction-averaged accelerated energetic proton distribution $f_0(x, p)$ at different particle energies as a function of the distance interval $x - x_0 \geqslant 0$, which is the distance downstream (in the direction of the solar wind flow) of the particle injection location at position $x_0 > 0$ from the Sun. The peak formation is displayed for a uniform SMFR domain stretching over a spatial interval of 0.3 au downstream of the injection point. The size of the SMFR interval is motivated by Figure 1, where the spatial peak formation in energetic particle fluxes in SMFR regions at 1 au is shown to occur during a time interval of ~20 hr within a 30 hr time frame, on average. Upon assuming that the observed SMFR fields are advected radially outward at a solar wind speed of 400 km s^{-1} (Zhao et al. 2018; Adhikari et al. 2019), a 20–30 hr time interval implies a spatial domain for SMFRs of about 0.2–0.3 au.

All of the curves for different particle energies are normalized to a value of 1 at the injection position when $x - x_0 = 0$. Thus, the maximum values of f_0 directly indicate the maximum amplification factors of f_0 relative to the particle injection location for different particle energies inside the SMFR region. Given that the particle distribution $f_0(p)$ is proportional to the differential intensity $j_T(T)$ ($j_T(T) = p^2 f_0(p)$, where T is the kinetic energy of the particle), the amplification factors of normalized $f_0(p)$ also serve as the amplification factors of j_T. Thus, the figure can be compared to observations of the amplification factor of particle differential intensity (or flux) at different energies in Figure 1. In our figure, the different color curves represent the amplification factors for energetic protons with kinetic energies 144 keV (black), 256 keV (red), 0.44 MeV (blue), 0.81 MeV (green), 1.44 MeV (yellow), and 3.31 MeV (cyan), thus falling inside the different detector energy intervals in Figure 1(a). To connect these particle energies to the values for the ratio p/p_0 in the analytical solution, we assumed that the injection momentum in the solar wind frame $p_0 = 400$ km s^{-1}, which is ~1 keV for protons. Thus, in the analytical solution, p/p_0 had to be varied between 12 and 57.5 to calculate the spatial curves shown in Figure 2

(left panel) for different particle kinetic energies that vary between between 144 keV and 3.31 MeV.

Figure 1 suggests that the observed average maximum amplification factor in the flux of energetic ions in the vicinity of 126 current sheet events at 1 au varies between ∼4.5 and 7.5 in the energy range 0.112–4.75 MeV (LEMS30 detector of the EPAM instrument on the *ACE* spacecraft), and between ∼3.5 and 5.5 in the energy range 0.066–4.75 MeV (LEMS120 detector of EPAM) with the largest amplification factor occurring at the highest energies. Peaks in the intensity enhancement appear to occur ∼11 hr or ∼0.11 au after the current sheet event without a clear energy dependence. The analytical results in Figure 2 (left panel) show that we can potentially reproduce the observations because the intensity amplification factor varies between ∼2.8 and 5.4 for particle energies in the range 0.144–3.31 MeV, thus increasing with energy. However, the theory also predicts a systematic shift in the peak enhancement varying from ∼0.05 to 0.1 au from low to high particle energies downstream of the injection point that does not appear to be present in the observations averaged over many events in Khabarova & Zank (2017). On the other hand, such a shift does appear in energetic ion observations of SMFR acceleration behind a traveling shock from the *Ulysses* spacecraft reported at 5 au (Zhao et al. 2018) and from the *Voyager 2* spacecraft behind the solar wind termination shock (Zank et al. 2015), although in the latter case the existence of an SMFR acceleration region still needs confirmation.

In Figure 2 (right panel), we present the corresponding accelerated energetic proton spectra from our analytical solution for second-order Fermi acceleration at the particle injection point $x - x_0 = 0$ (solid black curve) and at the following distances farther downstream: 0.05 au (solid red curve), 0.1 au (solid blue curve), 0.15 au (dashed green curve), 0.2 au (dashed cyan curve), and 0.25 au (dashed magenta curve). The spectra are normalized so that the distribution function at the injection point $x - x_0 = 0$ has a value of 1 at the lowest momentum shown ($p/p_0 = 1.5$, where p_0 is the injection momentum). At the particle injection location, the accelerated spectrum is close to a power law, being slightly softer than $f_0(p) \propto p^{-5}$ (in terms of differential intensity, it is somewhat harder than $j_T(T) \propto T^{-1.5}$) except at the lowest momenta where the spectrum steepens somewhat. Inspection of the spectral evolution with increasing distance downstream of the injection point reveals that the spectra become progressively harder and more exponential so that spectra at low energies are considerably harder compared to high energies. If one would fit a power law to the exponential spectrum at 0.2 au downstream of the injection location (dashed cyan curve), the spectrum would be approximately $f_0(p) \propto p^{-4}(j_T(T) \propto T^{-1})$ above ∼100 keV ($p/p_0 > 10$). This basic trend of spectral hardening and increasing exponential nature of accelerated proton spectra produced by SMFRs with increasing distance inside the SMFR region is consistent with SMFR acceleration events observed at 1 au reported by Adhikari et al. (2019). The variation in the power-law index through the SMFR region from ∼−1.5 to ∼−1 for particle energies ∼100 keV $< T <$ 1 MeV in the second event discussed by Adhikari et al. (2019) is close to the result reported here. A similar hardening trend in the energetic particle spectra through an SMFR region at ∼5 au was detected in *Ulysses* data as reported by Zhao et al. (2018) and Zhao et al. (2019).

9.1.2. SMFR Parameters Specified

Consider the SMFR parameters we had to specify to achieve the reasonably realistic results presented in Figure 2 (see Table 1). We used an Alfvén ratio of $r_A^I = 0.3$. Adhikari et al. (2015) reported observed values for the turbulence Alfvén ratio ranging between ∼0.1 and 0.6 in the vicinity of 1 au. Based on the nearly incompressible MHD (NI MHD) turbulence theory of Zank et al. (2017), inner heliospheric solutions of the coupled transport equations for the leading-order quasi-2D turbulence component, which contains magnetic island structures as a nonlinear component, and a minor parallel propagating Alfvén wave slab turbulence component yielded results supporting an Alfvén ratio less than 1 for SMFR turbulence in the solar wind at Earth orbit. It was predicted to be ∼0.1 when shear flow between fast and slow streams in the solar wind acts as a source for the magnetic fluctuations of quasi-2D turbulence.

We specified an SMFR normalized cross-helicity value of $\sigma_c^I = 0.1$ in the solution. Observations of this parameter (Adhikari et al. 2015) indicate a wide range of values near 1 au between ∼−0.1 and 0.8 so that the value we used falls safely within the broad observed range. The theoretical NI MHD turbulence solutions in Zank et al. (2017) suggest that a value of $\sigma_c^I \approx 0.2$ is possible near 1 au when shear flow acts a source for the magnetic fluctuations of 2D turbulence. In our solutions, we also specified an SMFR width or cross section of $L_I = 0.004$ au. This fits within the range of typical values of $L_I < 0.01$ au reported for SMFRs identified in the solar wind near 1 au (Khabarova et al. 2015, 2016). For the length of SMFRs, it was assumed that $L_{I\parallel} = 3L_I = 0.012$ au. Weygand et al. (2011), e.g., reported that the ratio of the parallel to perpendicular turbulence correlation lengths can be ∼2.6 with respect to the mean magnetic field direction. Because Hu et al. (2018) found SMFRs to be aligned with the Parker magnetic field direction and 2D SMFR turbulence is thought of as the dominant turbulence component in the solar wind near 1 au (e.g., Matthaeus et al. 1990; Bieber et al. 1994; Zank et al. 2017), one might interpret the Weygand et al. (2011) result for the ratio of parallel to perpendicular turbulence correlation lengths as supporting evidence for our assumption that $L_{I\parallel}/L_I = 3$. Furthermore, we assumed an enhanced Alfvén speed of $V_{A0} = 120$ km s^{-1}, which is a factor of 3 higher than a typical background value of 40 km s^{-1} at 1 au. This is motivated by the fact that many of the energetic particle intensity enhancements analyzed in Khabarova & Zank (2017) are thought of as occurring inside ICME structures where the magnetic field strength is considerably enhanced. Finally, we assumed that for SMFRs inside ICME structures, $\langle \delta B_I^2 \rangle / B_0^2 = 1$ near 1 au. Based on the superposed epoch analysis of SMFRs near the HCS (Cartwright & Moldwin 2010) and on the turbulence data analysis by Smith et al. (2016), it appears that a reasonable value for SMFRs is $\langle \delta B_I^2 \rangle / B_0^2 = 0.2$. This suggests that there is relatively considerably less energy in the twist or magnetic island component of SMFRs than we assumed in our solution. However, the referenced data analysis efforts did not target SMFRs in ICME regions specifically, so that it cannot be ruled out that SMFRs generated in the enhanced magnetic fields of ICMEs might indeed have a relatively stronger magnetic island component, but more data analysis needs to be done to verify this prediction. In conclusion, the SMFR parameters specified in our analytical solution can be considered reasonable in terms of the little that

Table 1
SMFR Parameters for the Second-order Fermi Acceleration Solution

r_A^I	σ_c^I	L_I (au)	$L_{I\parallel}$ (au)	V_{A0} (km s^{-1})	$\langle \delta B_I^2 \rangle / B_0^2$
0.3	0.1	0.004	0.012	120	1

is known about the statistics of SMFR parameters, but clearly more data analysis is needed to further refine these parameters.

If one studies the asymptotics of the analytical steady-state solutions in Section 8.1 for each type of SMFR acceleration mechanism, it can be seen that these test particle solutions only become insensitive to the SMFR parameters in the limit of strong acceleration. However, the predicted spectral slopes of the particle distribution are then also much harder compared to the observed spectra of accelerated particles in the SMFR regions discussed above that we try to model. Thus, our modeling activity occurs in an SMFR parameter regime where the analytical solutions are sensitive to the SMFR parameters specified. Our modeling experience shows that changes in SMFR parameters considerably smaller in factor than their large uncertainty discussed above can result in solutions that deviate far from the solutions and the associated observations presented in this paper. If one can specify reasonable SMFR parameters belonging to the regime of strong acceleration that require self-consistent acceleration modeling, we cannot rule out that such a self-consistent modeling approach could also produce realistic steepened particle spectra in a parameter regime where the modeling results are less sensitive to changes in SMFR parameters. Therefore, it is important that in future work, acceleration will be modeled self-consistently by solving the coupled focused and SMFR transport equations presented in Le Roux et al. (2018).

9.1.3. Second-order Fermi Acceleration and Other Transport Parameters

Based on the parameters specified, $D_{\rm INC}^{\rm Istoch} = 3D_{\rm COM}^{\rm Istoch}$. This means that second-order Fermi acceleration due to random fluctuations in the parallel shear flow of SMFRs (fluctuations in the incompressible or magnetic island area conserving contraction velocity) dominates second-order Fermi acceleration induced by random fluctuations in the compression rate of SMFRs. This domination is largely due to relaxing the strong guide field assumption used in deriving our acceleration expressions by specifying $\langle \delta B_I^2 \rangle / B_0^2 = 1$, which means that we are assuming that our theory is sufficiently accurate when the guide field is not dominant. Consider now $D_{\rm REC}^{\rm Istoch}$, which represents second-order Fermi acceleration generated by fluctuations in the parallel reconnection electric field produced by the merging of SMFRs (note that this acceleration effect has not been included in our analytical solution for second-order Fermi acceleration as discussed in Section 9.1.1). We find that for the range of particle speeds $1 < v/U_0 < 100$ (proton kinetic energies 1 keV $< T <$ 10 MeV), $D_{\rm REC}^{\rm Istoch}/D_{\rm INC}^{\rm Istoch}$ varies from $\sim 9.6 \times 10^6$–9.6×10^2 from low to high speeds, indicating that $D_{\rm REC}^{\rm Istoch}$ is the dominant stochastic acceleration mechanism for all energetic particle speeds of interest. However, such efficient acceleration is not expected to yield realistic spatial amplification factors for the accelerated energetic particle distribution at 1 au such as that displayed in Figure 2 (left panel), showing the need to reduce $D_{\rm REC}^{\rm Istoch}$. There are different possibilities: (1) the mean parallel reconnection electric field that forms when SMFRs are merging should be strongest in the local merging region between the SMFRs, thus yielding a much smaller large-scale average than assumed here. This might reduce $D_{\rm REC}^{\rm Istoch}$ to levels where $D_{\rm REC}^{\rm Istoch}$ is larger than $D_{\rm INC}^{\rm Istoch}$ and $D_{\rm COM}^{\rm Istoch}$ at lower particle speeds, but smaller than $D_{\rm INC}^{\rm Istoch}$ and $D_{\rm COM}^{\rm Istoch}$ at higher speeds. If so, the accelerated spectrum at the particle injection point would be less likely to form a power law as in Figure 2 (right panel). Then, accelerated particle spectra everywhere in the SMFR region will likely be exponential, which appears to be consistent with the spectra observed by Zhao et al. (2018, 2019) and Adhikari et al. (2019), which all show spectral hardening at lower energies. (2) We assumed in this solution that $\langle \delta B_I^2 \rangle / B_0^2 = 1$ in SMFR acceleration regions. If this value is inflated (see discussion in Section 9.1.2) so that SMFRs inside distorted ICMEs at 1 au are also in the strong guide field limit, all the stochastic acceleration mechanisms will be less efficient. In this case, $D_{\rm COM}^{\rm Istoch} \gg D_{\rm INC}^{\rm Istoch}$, and taking into account factor (1), perhaps $D_{\rm COM}^{\rm Istoch} > D_{\rm REC}^{\rm Istoch}$ at higher particle speeds but not at lower particle speeds. However, then all the acceleration mechanisms might not be efficient enough to reproduce realistic spatial amplification factors in SMFR acceleration regions at 1 au. Disregarding factor (1), $D_{\rm REC}^{\rm Istoch}$ is expected to still be too strong to produce realistic results. (3) Overly efficient $D_{\rm REC}^{I}$ acceleration can be counteracted by extending calculations to the nonlinear limit where the self-consistent energy exchange between energetic particles and SMFRs is modeled as was discussed in Le Roux et al. (2016, 2018).

The parallel diffusion coefficient is based on a nonlinear theory in which particles following the magnetic field experience pitch-angle scattering from random magnetic mirroring forces inside dynamic SMFRs so that they are effectively diffusing through SMFRs at the background Alfvén speed V_{A0} along the guide field with a parallel mean free path which is of the order of the length $L_{I\parallel}$ of SMFRs in the guide field direction (see Equation (33)). This nonlinear model suggests that energetic particles are diffusing slowly because, being trapped by the mirroring forces inside SMFRs, they are basically advected with the SMFR flow. However, to achieve the realistic results shown in Figure 2 required the parallel diffusion coefficient to be strongly enhanced by a factor of $\sim$58, indicating more effective diffusion through the SMFR field. This implies that particle diffusion through SMFRs due to scattering by mirroring forces should instead be modeled in the quasi-linear theory limit, but then the parallel diffusion would depend on particle speed, which is beyond the scope of our constant coefficient analytical solution. If we would specify the reduction $\langle \delta B_I^2 \rangle / B_0^2 = 0.1$ in both the parallel diffusion and second-order Fermi diffusion coefficients, we estimate that, to retain the values for the second-order Fermi acceleration and parallel diffusion coefficients that led to realistic energetic proton flux amplification factors, it would require boosting parallel diffusion by much smaller factors in the range of $\sim$3–5. Then, parallel diffusion is less likely to be in the quasi-linear limit of our theory, thus raising the probability that some particle trapping in SMFR structures occur.

The achieved realistic results displayed in Figure 2 also required significant particle escape from the SMFR region (Zhao et al. 2018) because we had to specify $\tau_{\rm esc}/\tau_{\kappa_0^I} = 1.7$, where $\tau_{\kappa_0^I} = \kappa_0^I / U_0^2$ is the diffusion timescale. The escape softened the accelerated energetic particle spectra in the SMFR region to better reflect observations, such as those reported by

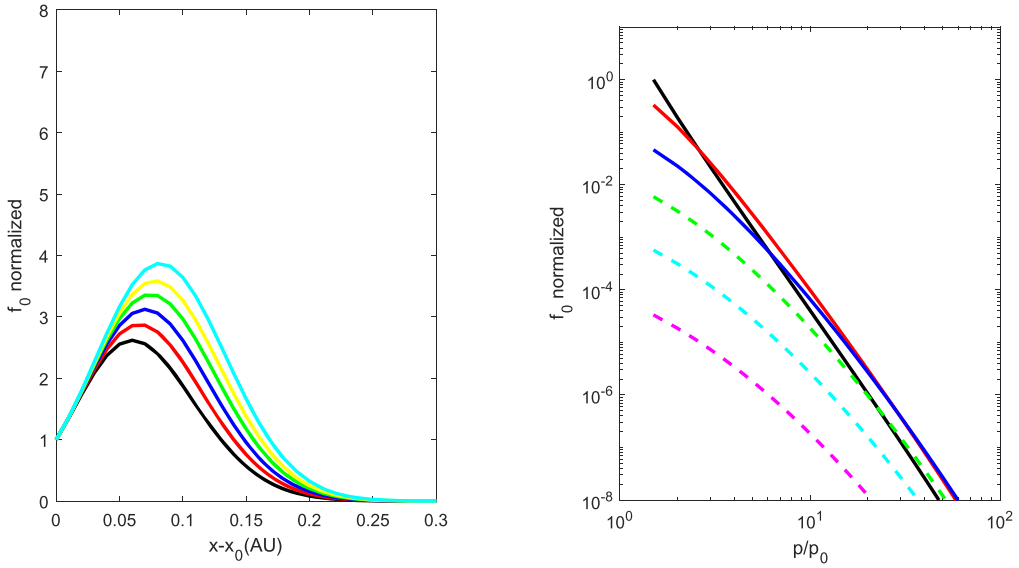

Figure 3. The 1D time-dependent solution of the diffusive Parker transport equation for energetic proton second-order Fermi acceleration in a uniform SMFR region in the vicinity of 1 au (Equation (22)). As in Figure 2, the solution combines second-order Fermi acceleration due to the variance in the SMFR compression rate and in the SMFR incompressible parallel shear flow. The parameters specified in the time-dependent solution are identical to parameters used to produce the steady-state solution in Figure 2. The results show the solution after ∼10.4 hr of acceleration. Left panel: the same format as Figure 2 (left panel). Right panel: same as Figure 2 (right panel).

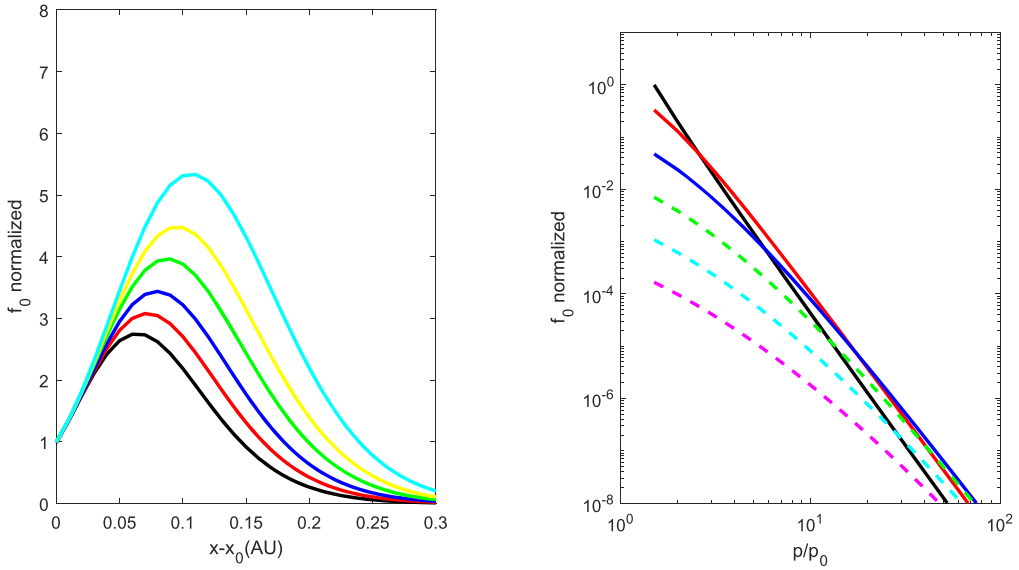

Figure 4. The 1D time-dependent solution of the diffusive Parker transport equation for energetic proton second-order Fermi acceleration in a uniform SMFR region in the vicinity of 1 au (Equation (22)). As in Figure 2, the solution combines second-order Fermi acceleration due to the variance in the SMFR compression rate and in the SMFR incompressible parallel shear flow. The parameters specified in the time-dependent solution are identical to parameters used to produce the steady-state solution in Figure 2. The results show the solution after ∼20.8 hr of acceleration. Left panel: the same format as Figure 2 (left panel). Right panel: same as Figure 2 (right panel).

Zhao et al. (2018, 2019) and Adhikari et al. (2019). That does not mean that only escape is responsible for softening the accelerated particle spectra, but it could be an indication that the accelerated energetic particles extracted enough energy from SMFRs to significantly weaken these structures, pointing toward the need for a self-consistent acceleration approach (Le Roux et al. 2016, 2018).

9.1.4. Time-dependent Diffusive Solutions

We discuss the feasibility of using a steady-state solution to compare with observations by studying time-dependent solutions of the diffusive Parker transport equation, that is, time-dependent solutions where the telegrapher term (first term in Equation (14)) is ignored. The time-dependent solution is given by Equation (22) in which we set $\langle \nu^I_{\rm COM} \rangle$, U^I_E, and $D^{\rm Icoh}_{pp}$ in D^I_0 to zero to remove acceleration by mean SMFR fields because the focus is on second-order Fermi acceleration by SMFRs associated with the variance in SMFR fields ($p^2 D^I_0 = D^{\rm Istoch}_{pp}$). The results in Figure 3 show the solution after ∼10.4 hr of acceleration, whereas those in Figure 4 represent the solution after ∼20.8 hr of acceleration. Comparison of these results with the steady-state results shown in

Figure 2 indicates that the time-dependent results in Figure 4 reached a steady state within the spatial domain and momentum interval of interest. Thus, it takes between ∼10 and 21 hr of acceleration before a steady state occurs.

As discussed above, it appears from the superposed epoch analysis of many SMFR acceleration events in Khabarova & Zank (2017) that the average duration of an SMFR acceleration region at 1 au is ∼20–30 hr. This implies a mean radial SMFR region size of ∼0.2–0.3 au assuming that SMFRs are advected radially outward at a solar wind speed of ∼400 km s^{-1} (Zhao et al. 2018; Adhikari et al. 2019). If we approximate the acceleration time to reach a steady state to be ∼15 hr, it would imply that we have to inject particles into the SMFR region at radial distances less than ∼0.55–0.65 au from the Sun to ensure that a steady-state peaked spatial profile for accelerated energetic particles with a width of 0.2–0.3 au are advected past the observer at 1 au. This does require, however, that particle injection occurring beyond 0.55–0.65 au is of negligible importance compared to those injected inside 0.55–0.65 au, which is a reasonable assumption given the effect of spherical expansion on reducing potential particle sources with increasing heliocentric distance. Furthermore, considering injected particle transport over a radial distance of ∼0.5 au to Earth, the assumption of spatially uniform coefficients in the analytical solution is a concern, and a solution depending on heliocentric radial distance might be necessary. Thus, reproducing observations of energetic particles accelerated by SMFRs with steady-state planar analytical solutions should be seen as the first approximate step toward a more realistic time-dependent spherically symmetric solution with radially dependent transport coefficients and particle injection throughout the SMFR region that will be attempted in future work.

9.1.5. Telegrapher Time-dependent Solutions

In this section, we compare the time-dependent diffusive solution (Equation (22)) with the telegrapher solution (Equation (19)). We find that at later times, when both kinds of time-dependent solutions settle into steady state, the results of the telegrapher solution agrees well with the time-dependent diffusive solution within the specified SMFR spatial domain downstream of the particle injection position and momentum interval for energetic protons. This can be seen in the good agreement between the telegrapher solution results for spatial peak formation in the distribution function f_0 in Figure 5 and the time-dependent diffusive solution in Figure 4 (left panel), both cases representing ∼20 hr worth of second-order Fermi acceleration. As before, the results cover a spatial domain of 0.3 au downstream of the particle injection position at $x - x_0 = 0$ for different proton kinetic energies ranging from 144 keV to 3.31 MeV (see caption of Figure 2 (left panel)).

The differences between the two types of time-dependent solutions can be best illustrated earlier during acceleration. In Figures 6 and 7, telegrapher solutions and time-dependent diffusive solutions are compared for a much shorter acceleration time of ∼3.1 hr. For information about the various curves, see the caption of Figure 2. Consider the difference between the energetic proton spatial profiles for the telegrapher solution (Figure 6, left panel) and time-dependent diffusive solution (Figure 6, right panel). As expected, the telegrapher solution imposes a cutoff on the maximum distance of diffusive particle propagation downstream of the injection point at

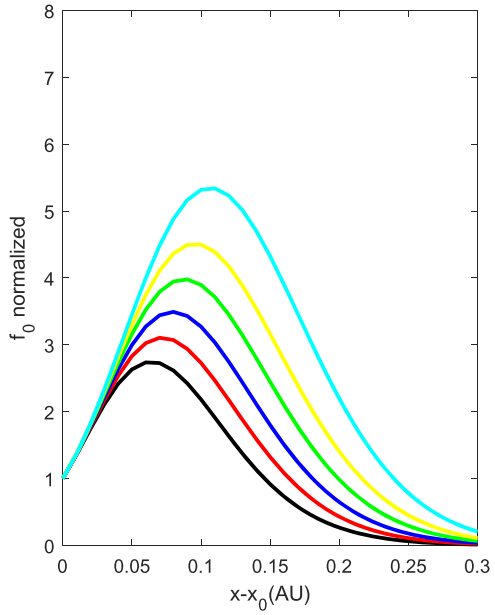

Figure 5. The 1D time-dependent solution of the telegrapher Parker transport equation for energetic proton second-order Fermi acceleration in a uniform SMFR region in the vicinity of 1 au (Equation (19)). As in Figure 2, the solution combines second-order Fermi acceleration due to the variance in the SMFR compression rate and in the SMFR incompressible parallel shear flow. The parameters specified in the time-dependent solution are identical to parameters used to produce the steady-state solution in Figure 2. The results show the solution after ∼20.8 hr of acceleration. The figure is in the same format as Figure 2 (left panel).

$x - x_0 = 0$ whereas in the time-dependent diffusive solution there is no cutoff, only a gradual rollover. We also notice that the spatial cutoffs shift increasingly farther downstream of the injection point with increasing particle energy in the telegrapher solution. This is consistent with the causality cutoff condition in the telegrapher solution (Equation (19)),

$$\frac{1}{3}v^2(t - t_0)^2 \geqslant (x - x_0)^2 + \frac{\kappa_0^I}{D_0^I}\ln^2\left(\frac{p}{p_0}\right), \tag{36}$$

which indicates that faster propagating leading diffusive (nearly isotropic) particle pulses can propagate farther downstream in a given time.

Compare the evolution of the accelerated energetic particle spectra with increasing distance inside the SMFR region for the telegrapher solution (Figure 7, left panel) and the time-dependent diffusion solution (Figure 7, right panel). The results reveal that the telegrapher solution also imposes momentum cutoffs in the spectra at lower particle energies in accordance with causality condition (36) whereas the diffusive solution exhibits a gradual spectral rollover without a cutoff at lower particle energies. In the telegrapher solution, the momentum cutoffs at lower energies occur at progressively higher particle momenta with increasing distance downstream of the particle injection position as predicted by Equation (36) (only the faster propagating leading diffusive particle pulse can reach the observer at larger distances downstream in a given time). At later times, the spatial and momentum cutoffs disappear from the displayed solutions (e.g., Figure 5) because they shift outside the spatial and momentum intervals of interest.

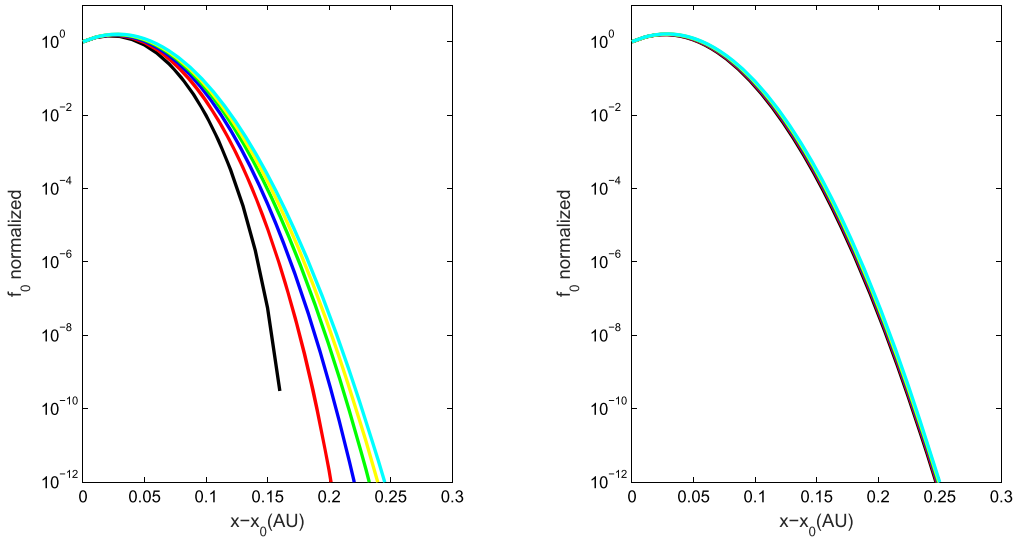

Figure 6. Early-time comparison of the 1D time-dependent solution of the telegrapher Parker transport equation with the 1D time-dependent solution of the diffusive Parker transport equation for energetic proton second-order Fermi acceleration in a uniform SMFR region in the vicinity of 1 au. As in Figure 2, the solution combines second-order Fermi acceleration due to the variance in the SMFR compression rate and in the SMFR incompressible parallel shear flow. The parameters specified in the time-dependent solutions are identical to the parameters used to produce the steady-state solution in Figure 2. The results show the solution after ∼3.1 hr of acceleration. Left panel: solution of the telegrapher Parker transport equation. Right panel: solution of the time-dependent diffusive Parker transport equation. Both panels follow the same format as Figure 2 (left panel) except that the distribution function f_0 is plotted on a logarithmic scale in this figure to enhance visibility of the cutoff in the spatial profiles far downstream of the injection point at $x - x_0 = 0$ au. The different color curves cannot be clearly distinguished in the right panel because of overlap.

9.2. First-order Fermi Acceleration due to the Particle Scattering in Mean SMFR Fields

Now we consider the first-order Fermi acceleration of energetic ions in response to the mean compression rate of SMFRs in an SMFR region at 1 au. Our goal is to see whether this SMFR acceleration mechanism, which played a prominent role in reproducing observations of energetic particle acceleration at both 1 and 5 au (Zhao et al. 2018; Adhikari et al. 2019), can still potentially do so when reasonable SMFR parameters are specified at 1 au. For this mechanism, the average relative momentum rate of change of energetic particles is

$$\frac{1}{p}\left\langle \frac{dp}{dt} \right\rangle = -\frac{1}{3}\langle \nu^I_{\rm COM}\rangle, \tag{37}$$

where the expression for the mean SMFR compression rate is modeled according to the expression

$$\begin{aligned}\langle \nu^I_{\rm COM}\rangle &= \langle \nabla \cdot \delta \boldsymbol{U}^I_I\rangle \\ &= \sigma^I_{\rm COM}(r^I_{\rm A})^{1/2}\left(\frac{\langle \delta B^2_I\rangle}{B^2_0}\right)^{1/2}\frac{V_{\rm A0}}{L_I}.\end{aligned} \tag{38}$$

For more discussion on the bottom expression of Equation (38), see Appendix A.1 in Le Roux et al. (2018). In Equation (38), we specified $\sigma^I_{\rm COM} = +1$ for the case of maximum acceleration efficiency, that is, we assume that all SMFRs in the SMFR region are undergoing compression. In particle simulations, compression acceleration can be more important than shear-flow acceleration in SMFRs formed by magnetic reconnection at large-scale reconnecting current sheets when the guide field is sufficiently weaker than the reconnection magnetic field (Li et al. 2018). Global SMFR compression appears to occur when an interplanetary shock interacts with the HCS, and SMFRs, trapped between the converging primary current sheet at the leading edge of the ICME and the HCS, are compressed. Another possibility is that strong large-scale current sheets inside an ICME structure produce SMFRs through magnetic reconnection when these current sheets are disturbed through ICME compression between a pair of CIRs. The SMFRs thus generated experience compression from the surrounding CIRs (Adhikari et al. 2019).

In Figure 8, we present results for the steady-state solution of first-order Fermi acceleration of energetic protons by compressing SMFRs (see Equation (27)). The energetic proton distribution function amplification factors shown in Figure 8 (left panel) have the familiar pattern of the maximum factors being larger and shifted to larger distances downstream of the injection point at $x - x_0 = 0$ for higher-energy particles as we found for second-order Fermi acceleration. The amplification factors in the SMFR region have peak values close to those produced with second-order Fermi acceleration (see Figure 2 (left panel)). The results in Figure 8 (right panel) for accelerated energetic proton spectra, at the particle injection point and at different distances downstream of the injection location, also follow the same trend as for second-order Fermi acceleration (compare with Figure 2 (right panel)). As before, there is a power-law spectrum at the particle source (black curve), followed by spectra at larger distances beyond the source point that are harder overall as they bend over increasingly at lower particle energies with increasing distance beyond the source deeper inside the SMFR region. The spectra range from about $f_0 \propto p^{-5}$ for the distribution function or $j_T \propto T^{-1.5}$ for the differential intensity (flux) at the particle injection point (black curve) to approximately $f_0 \propto p^{-3}$ or $j_T \propto T^{-0.5}$ at 0.15 au downstream of the injection location (green dashed curve) when fitting a power law to the latter curve above ∼100 keV ($p/p_0 \geqslant 10$). In Figure 2 (right panel), the accelerated particle spectral intensity evolves from a power-law index somewhat smaller than ∼−1.5 at the injection point to reach a power-law index of ∼−1 at a distance of 0.2 au downstream (dashed cyan

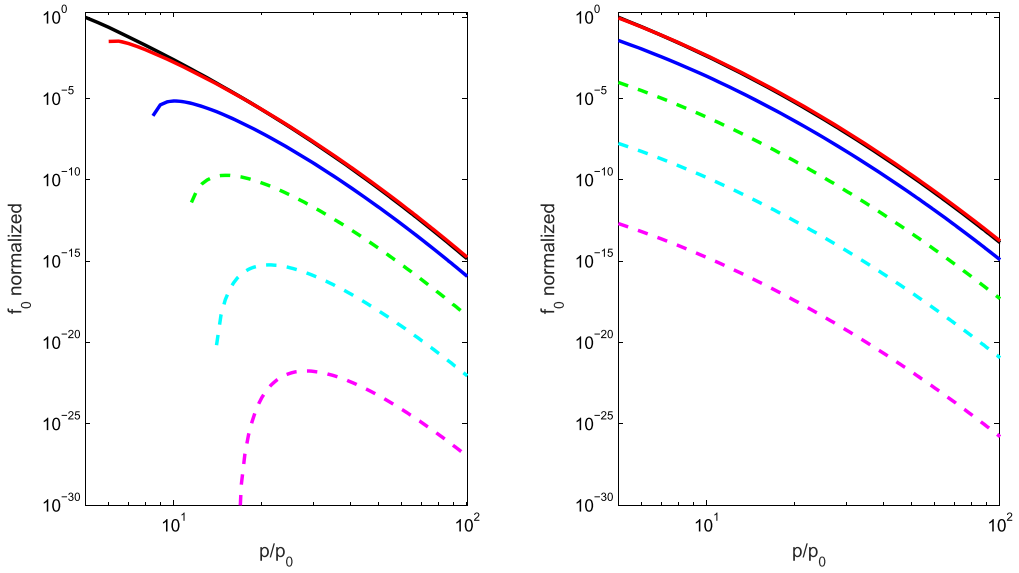

Figure 7. Early-time comparison of the 1D time-dependent solution of the telegrapher Parker transport equation with the 1D time-dependent solution of the diffusive Parker transport equation for energetic proton second-order Fermi acceleration in a uniform SMFR region in the vicinity of 1 au. As in Figure 2, the solution combines second-order Fermi acceleration due to the variance in the SMFR compression rate and in the SMFR incompressible parallel shear flow. The parameters specified in the time-dependent solutions are identical to parameters used to produce the steady-state solution in Figure 2. The results show the solution after ∼3.1 hr of acceleration. Left panel: solution of the telegrapher Parker transport equation. Right panel: solution of the time-dependent diffusive Parker transport equation. Both panels follow the same format as Figure 2 (right panel) except that the domain and range have been changed to better showcase the low-energy spectral cutoffs.

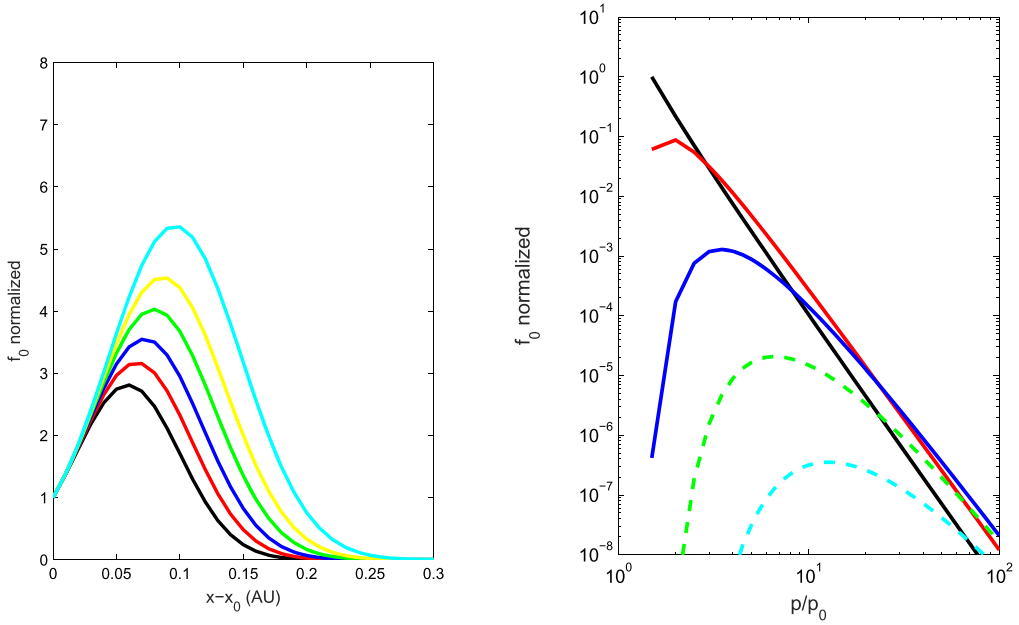

Figure 8. The 1D steady-state solution for energetic proton first-order Fermi or mean compression acceleration by SMFRs in a uniform SMFR region in the vicinity of 1 au (Equation (27)). Left panel: the same format as Figure 2 (left panel). Right panel: same format as Figure 2 (right panel).

curve) above 100 keV. Thus, the spectra for first-order Fermi acceleration become harder over shorter distances downstream of the injection point compared to the spectra in Figure 2 (right panel). Furthermore, we see that the accelerated energetic particle spectra produced with first-order Fermi acceleration roll over much more strongly at lower energies compared to the spectra produced by second-order Fermi acceleration downstream of the particle injection point, due to the cutoff in the downstream spectrum at the injection momentum (see the solution as given by Equation (27)). This illuminates a key difference between the first-order Fermi acceleration solution, where all the particles that arrive downstream of the injection point have been accelerated to momenta larger than the injection momentum to form the low-energy cutoff at the injection momentum, and the second-order Fermi solution, where particles arriving downstream experienced stochastic acceleration which lowers the probability for a low-energy cutoff at the injection momentum. This predicted difference in the spectral evolution for the two acceleration mechanisms downstream of the injection point might potentially be helpful for identifying the dominant operating SMFR acceleration mechanism in observations. Based on the evolution of the

Table 2
SMFR Parameters for the First-order Fermi Acceleration Solution

r_A^I	σ_c^I	L_I (au)	$L_{I\parallel}$ (au)	V_{A0} (km s^{-1})	$\langle \delta B_I^2 \rangle / B_0^2$
0.48	0.1	0.001	0.003	146	1

spectral power-law index through the SMFR region, in SMFR acceleration event two of Adhikari et al. (2019), the event with spectral indices closest to our results, the less strong spectral hardening for second-order Fermi acceleration is closer to the observed hardening trend. However, more SMFR acceleration events need to be studied before conclusions can be drawn with confidence.

9.2.1. SMFR and Energetic Particle Parameters Specified

An approximate reproduction of the average energetic ion flux amplification factors observed at 1 au presented in Figure 1 (see also Khabarova & Zank 2017) was accomplished by using SMFR parameters for first-order Fermi acceleration at 1 au that are the same or not very different from the reasonable parameters we used to simulate second-order Fermi acceleration at 1 au as discussed above (compare the SMFR parameters in Table 2 used to model first-order Fermi acceleration to those in Table 1 employed to model second-order Fermi acceleration). The exception is the cross section of 0.001 au specified for the SMFRs that is a factor of 4 smaller compared to the value used for second-order Fermi acceleration, but this value still fits in the typical range quoted for SMFR cross sections of ~0.01–0.001 au at 1 au (Cartwright & Moldwin 2010; Khabarova et al. 2015).

It was necessary to specify a parallel diffusion coefficient that is boosted by an additional factor of 5 relative to the enhanced value specified for second-order Fermi acceleration, emphasizing again that our nonlinear diffusion model for quasi-trapping of energetic particles by magnetic mirroring forces in SMFRs underestimates the efficiency of parallel diffusion through SMFRs. This suggests that pitch-angle scattering is considerably weaker inside SMFRs than predicted by our nonlinear theory so that the weak scattering (quasi-linear) limit of our parallel diffusion theory should be used to generate more efficient parallel diffusion. This option was not considered because our analytical solutions do not allow for velocity-dependent diffusion coefficients. We also needed the ratio of the parallel diffusion time over the escape time to have a value of $\tau_{DIF}/\tau_{esc} = (\kappa_0^I/U_0^2)/\tau_{esc} = 5$, which is five times the ratio used for second-order Fermi acceleration. Because the parallel diffusion coefficient is five times larger for first-order Fermi acceleration, it means that the same escape time was specified for both acceleration mechanisms.

10. Summary

In this paper, we presented new, more comprehensive analytical solutions of a diffusive and a telegrapher-type Parker transport equation for energetic particle acceleration in a solar wind region containing numerous dynamic SMFRs that unify all four SMFR acceleration mechanisms present in the underlying focused transport theory. The four acceleration mechanisms are SMFR compression acceleration, incompressible parallel shear-flow acceleration, and parallel guiding center motion acceleration by the parallel reconnection electric field force in merging SMFRs and by the parallel noninertial force associated with the acceleration of SMFR flow. More specifically, the new 1D analytical solutions combine first-order Fermi acceleration (acceleration by the mean SMFR compression), acceleration by the mean SMFR parallel reconnection electric field generated by merging SMFRs due to the mixed-derivative transport term in the Parker transport equation, and second-order Fermi SMFR acceleration. The second-order Fermi SMFR acceleration in our theory models two classes of acceleration, and each class contains contributions from all four SMFR acceleration mechanisms. Class one acceleration refers to energetic particles undergoing pitch-angle scattering while responding to mean SMFR fields, and class two acceleration has to do with particles responding to the variance in SMFR fields. Previous analytical solutions by Zank et al. (2014), Zhao et al. (2018), and Adhikari et al. (2019) unified the first two mechanisms but ignored second-order Fermi acceleration.

Besides new steady-state solutions, we present new time-dependent analytical solutions. For this purpose, we derived a new telegrapher Parker transport equation from the underlying focused transport equation for SMFR acceleration valid up to the second anisotropic moment of the particle distribution. An interesting feature of the telegrapher solution is that the strength of particle acceleration by the mean parallel reconnection electric field in merging SMFRs associated with the mixed-derivative transport term must be sufficiently constrained relative to second-order Fermi acceleration by SMFRs to fulfill the causality condition in the solution. Therefore, a solution of SMFR acceleration involving the mixed-derivative term is not viable without second-order Fermi acceleration, thus emphasizing the need to include the latter in SMFR acceleration studies. The causality condition in the telegrapher solution introduced cutoffs in the spatial profile of the accelerated particle distributions at the maximum physically possible distances for diffusive propagation downstream of the particle injection point. The cutoff shifted to larger downstream distances with increasing particle energy in a given acceleration time. In addition, momentum cutoffs were imposed by the causality condition in the accelerated particle spectra downstream of the injection location at lower particle energies. These low-energy cutoffs shifted toward higher particle energies with increasing distances downstream of the injection location. These cutoffs are only visible during early acceleration times because during later times, they shift outside the spatial and momentum interval of interest. A simplified, diffusive time-dependent solution (without telegrapher effects) that agrees with the steady-state solution and approximately agrees with the telegrapher solution in the spatial and momentum interval of interest at late times was also presented.

Inspection of the complete steady-state solution clearly showed the basic trends in observed SMFR acceleration events, such as spatial peak formation in the distribution function downstream of the particle injection location, and accelerated particle spectra that hardens and bends over increasingly at lower energies with increasing distance downstream of the injection point that is consistent with previous analytical solutions (Khabarova & Zank 2017; Zhao et al. 2018, 2019; Adhikari et al. 2019). Further analysis of the steady-state solution at the injection position revealed that, in the test particle limit, first-order Fermi or SMFR compression acceleration produced the hardest spectrum (a very flat power-law

spectrum), followed by acceleration by the mean parallel reconnection electric field in merging SMFRs through the mixed-derivative transport term (the distribution function $f_0(p) \propto p^{-3/2}$ (Zank et al. 2014)), while second-order Fermi SMFR acceleration yielded the softest accelerated spectrum of $f_0(p) \propto p^{-3}$ (Le Roux et al. 2015)). Further noteworthy features of the steady-state solution are that the low-energy bend-over in the accelerated spectrum downstream of the particle injection location cuts off at the injection momentum in the case of first-order Fermi acceleration, and that the mixed-derivative acceleration term is the only one that does not produce a peak in the downstream accelerated particle distribution (a plateau is formed as shown by Zank et al. 2014).

Armed with these solutions, we explored the possibility of reproducing observations of accelerated energetic proton flux enhancements and spectral evolution in active SMFR regions at 1 au using reasonable SMFR parameters. For this purpose, we used as a guide observations of accelerated energetic protons in SMFR regions at 1 au as presented in Khabarova & Zank (2017; see Figure 1) and in Adhikari et al. (2019). Previously, Zhao et al. (2018) and Adhikari et al. (2019) had success in reproducing SMFR acceleration event characteristics both at 1 and ~5 au with steady-state analytical solutions in which first-order Fermi SMFR compression acceleration appears to be the dominant acceleration mechanism, but without connecting the acceleration and transport timescale SMFR properties. The solution also included a term for particle escape out of the SMFR region to avoid producing accelerated particle spectra that are harder than the observed spectra; second-order Fermi SMFR acceleration was not considered.

Initial results showing flux amplification and spectral hardening for second-order Fermi SMFR acceleration were first presented in Le Roux et al. (2015, 2016), but without attempting to reproduce any observations. The results in this paper represented our first attempt to achieve a realistic rendition of observed SMFR acceleration features near 1 au with second-order Fermi SMFR acceleration. The key point of the results in Figures 2–7 in this paper is that one can potentially also reproduce the observed flux amplification of energetic ions as a function of particle energy and the evolution of the accelerated spectra through SMFR regions at 1 au by focusing solely on second-order Fermi acceleration of energetic ions in response to statistical fluctuations (variance) in SMFR fields, and that this can be accomplished with reasonable SMFR parameters. Realistic results for flux amplification and spectral hardening were achieved with second-order Fermi acceleration that combines the acceleration effects associated with the variance in SMFR compression and in SMFR incompressible parallel shear flow. Second-order Fermi acceleration by the variance in the parallel reconnection electric field in merging SMFRs was not included in the modeling efforts because for this mechanism, the acceleration parameter $D_0^I = D_{pp}/p^2$ for second-order Fermi acceleration in the solution depends on particle speed and our analytical solutions only holds for D_0^I being a constant. Nonetheless, based on the SMFR parameters that we specified in the modeling efforts, we estimated that stochastic acceleration by the variance in the reconnection electric field is the dominant second-order Fermi acceleration mechanism, followed by acceleration involving the variance in incompressible parallel shear flow, which, due to the variance in SMFR compression, is the least efficient. However, due to our limited knowledge of the SMFR parameters that enter into the acceleration expressions, and because of limitations of the analytical solutions, it is difficult to draw definitive conclusions about the ranking of the different second-order Fermi acceleration mechanisms associated with the variance in SMFR fields. This points to the need to intensify our data analysis of SMFR acceleration events, while at the same time increasing the sophistication of the solutions.

Interestingly, we found that we needed to specify parallel diffusion that is considerably more efficient than predicted by our nonlinear theory for parallel diffusion if we want to reproduce observations at 1 au with second-order Fermi SMFR acceleration. Thus, our model for parallel diffusion, where particles are scattered by random magnetic mirroring forces in SMFRs, should be applied in the quasi-linear diffusion limit so that quasi-trapping of particles in SMFRs is insignificant. On the other hand, we estimated that the required factor of enhancement in parallel diffusion drops substantially when the ratio of the mean energy density of the island or twist component over the axial or guide field component of SMFRs is reduced. Furthermore, it still needs to be investigated whether analytical solutions in spherical geometry, which is a more appropriate geometry for the expanding solar wind, will yield a different result for parallel diffusion, a matter that will be investigated in future research.

We illustrated with our results for first-order Fermi acceleration by compressing SMFRs in Figure 8 that we can generate results for peak formation in the energetic particle distribution downstream of the particle injection point that are remarkably similar to those based on second-order Fermi acceleration in which the variance of the parallel shear flow in SMFRs played a dominant role. Thus, with both first- and second-order Fermi SMFR acceleration, the observed enhanced energetic ion flux in SMFR regions at 1 au from Khabarova & Zank (2017; see Figure 1 in this paper) were reproduced reasonably well with acceptable SMFR parameters. The SMFR parameters specified in the first-order Fermi solution closely follow those used in the second-order Fermi solution, except for the characteristic cross section of SMFRs that was reduced by a factor of 4. However, the reduced value is within the range of possibility. This indicated that we do not know enough about the statistics of SMFR parameters in SMFR acceleration regions in the solar wind to distinguish between first- and the various second-order Fermi SMFR acceleration mechanisms, which stressed the need for more detailed analysis of SMFR properties in SMFR acceleration regions.

Similar to the results for second-order Fermi acceleration, the accelerated spectra for first-order Fermi acceleration were power laws at the particle injection point and exhibited the same rollover trend qualitatively at lower particle energies downstream of the injection point (see also, Zhao et al. 2018; Adhikari et al. 2019). However, the spectral rollover trend at lower particle energies and overall increasing spectral hardening downstream of the injection location were notably stronger in the case of first-order Fermi acceleration, due to the cutoff in the downstream spectrum at the injection momentum. This illuminates a key difference between the first-order Fermi acceleration solution, where all the particles that arrive downstream of the injection point have been accelerated to momenta larger than the injection momentum to form the low-energy cutoff at the injection momentum, and the second-order Fermi solution where particles arriving downstream experienced stochastic acceleration which lowers the probability for a

low-energy cutoff at the injection momentum. This predicted difference in the spectral evolution for the two acceleration mechanisms downstream of the injection point might potentially be helpful for identifying the dominant operating SMFR acceleration mechanism in observations. Based on the evolution of the spectral power-law index through the SMFR region in SMFR acceleration event two of Adhikari et al. (2019), the event with spectral indices closest to our results, the less strong spectral hardening in the second-order Fermi acceleration case is closer to the observed hardening trend. More SMFR acceleration events need to be studied before conclusions can be drawn with confidence.

The success of our SMFR acceleration results for both first-order Fermi acceleration (see also Zhao et al. 2018; Adhikari et al. 2019) and second-order Fermi acceleration required a term for the rate of particle escape from the SMFR region to ensure steepened accelerated particle spectra with more realistic slopes. However, it must be noted that the need for steeper accelerated spectra in the solution can partly be the result of modeling particle acceleration in the test particle limit. The considerable pressure in the accelerated test particle spectra indicates that the energy exchange between the particles and SMFRs should be modeled self-consistently, thus also contributing to steeper accelerated particle spectra (Le Roux et al. 2016, 2018).

J.A.l.R. acknowledges support from NASA Grants NNX15AI65G, 80NSSC19K027, NSF-DOE grant PHY-1707247, and NSF-EPSCoR RII-Track-1 Cooperative Agreement OIA-1655280. G.M.W. was partially supported by NASA grant 80NSSC19K0075, and O.V.K. by RFBR grants 16-02-00479, 17-02-00300, 17-02-01328, 18-52-06002, and 19-02-00957.

Appendix

A.1. Analytical Solution of the Telegrapher Parker Transport Equation

The telegrapher Parker equation for the evolution of the isotropic part of the energetic particle distribution function $f_0(x, p, t)$ we want to solve analytically (see Equation (14) and its discussion in Section 6) is given by

$$\tau_{\rm sc}^I\frac{\partial^2 f_0}{\partial t^2}+\frac{\partial f_0}{\partial t}+U_0^I\frac{\partial f_0}{\partial x}+\frac{1}{3}\langle\nu_{\rm COM}^I\rangle p\frac{\partial f_0}{\partial p}=\kappa_{xx}^{I1}\frac{\partial^2 f_0}{\partial x^2}+\frac{1}{p^2}\frac{\partial}{\partial p}\left(p^2D_{pp}^I\frac{\partial f_0}{\partial p}\right)+\frac{2}{3}U_E^I\frac{\partial}{\partial x}\left(p\frac{\partial f_0}{\partial p}\right)-\frac{f_0}{\tau_{\rm esc}}+Q, \quad (39)$$

where $\tau_{\rm sc}^I$ is the particle scattering time, $U_0^I=U_0-U_E$ (U_0 is the solar wind flow speed and U_E^I is an advection speed associated with the mean parallel reconnection electric field) is an the effective advection speed in the x direction, $\langle\nu_{\rm COM}^I\rangle$ is the mean SMFR compression rate, $\kappa_{xx}^I=\kappa_0^I=\kappa_\parallel^I\cos^2\psi$ ($\kappa_\parallel^I$ is the parallel diffusion coefficient and ψ is the interplanetary magnetic spiral field angle) is the diffusion coefficient in the x direction, $D_{pp}^I=p^2D_0^I$ is the total momentum diffusion coefficient for second-order Fermi acceleration by SMFRs, $-f_0/\tau_{\rm esc}$ is a loss term acting on a characteristic timescale $\tau_{\rm esc}$, and Q is a point source of N_0 energetic particles injected with a momentum p_0 at position $x=x_0$ at time t_0 with the expression

$$Q(x,p,t)=\left(\frac{N_0}{4\pi p_0^2}\right)\delta(p-p_0)\delta(x-x_0)\delta(t-t_0). \quad (40)$$

Upon defining $z=\ln(p/p_0)$, Equation (39) can be expressed as

$$\tau_{\rm sc}^I\frac{\partial^2 f_0}{\partial t^2}+\frac{\partial f_0}{\partial t}+U_0^I\frac{\partial f_0}{\partial x}-\kappa_0^I\frac{\partial^2 f_0}{\partial x^2}+\left(\frac{1}{3}\langle\nu_{\rm COM}^I\rangle-3D_0^I\right)\frac{\partial f_0}{\partial z}-D_0^I\frac{\partial^2 f_0}{\partial z^2}-\frac{2}{3}U_E^I\frac{\partial}{\partial x}\left(\frac{\partial f_0}{\partial z}\right)+\frac{f_0}{\tau_{\rm esc}}=\left(\frac{N_0}{4\pi p_0^3}\right)\delta(z)\delta(x-x_0)\delta(t-t_0). \quad (41)$$

We apply the double Laplace transform

$$F_0(x,\eta,s)=\int_0^\infty dt e^{-st}\int_0^\infty dz e^{-\eta z}f_0(x,z,t) \quad (42)$$

to Equation (41) to eliminate the time and momentum derivatives. Because $z=\ln(p/p_0)$ varies from zero to infinity in the Laplace transform, it implies that p/p_0 varies from one to infinity. This indicates that we are only interested in studying the acceleration of source particles by SMFRs injected at $p=p_0$. The result is a second-order ODE with respect to x given by

$$\frac{d^2F_0}{dx^2}+\left(\frac{2/3U_E^I\eta-U_0^I}{\kappa_0^I}\right)\frac{dF_0}{dx}+\left(\frac{D_0^I\eta^2+(3D_0^I-\langle\nu_{\rm COM}^I\rangle/3)\eta}{\kappa_0^I}-\frac{s(\tau_{\rm sc}^Is+1)}{\kappa_0^I}-\frac{1}{\kappa_0^I\tau_{\rm esc}}\right)F_0=-\left(\frac{N_0}{4\pi p_0^3}\right)\frac{e^{-st_0}}{\kappa_0^I}\delta(x-x_0). \quad (43)$$

In deriving Equation (43), we specified the conditions $f_0(x,z,t=t_0)=0$, $\partial f_0/\partial t(x,z,t=t_0)=0$, $f_0(x,z=0,t)=0$, and $\partial f_0/\partial z(x,z=0,t)=0$. The solution of the homogeneous ODE in Equation (43) is

$$F_0(x)=C_1e^{\lambda_1x}+C_2e^{\lambda_2x}, \quad (44)$$

where

$$\lambda_{1,2}=\frac{1}{2}\left(\frac{U_0^I-2/3U_E^I\eta}{\kappa_0^I}\right)\pm\frac{1}{2}\left[\left(\frac{U_0^I-2/3U_E^I\eta}{\kappa_0^I}\right)^2-4\left(\frac{D_0^I\eta^2+(3D_0^I-1/3\langle\nu_{\rm COM}^I\rangle)\eta-s(\tau_{\rm sc}^Is+1)-1/\tau_{\rm esc}}{\kappa_0^I}\right)\right]^{1/2}, \quad (45)$$

requiring that $\mathrm{Re}(\lambda_1)>0$ and $\mathrm{Re}(\lambda_2)<0$. Following Morse & Feshbach (1981, p. 530), the solution of the inhomogeneous

ODE in Equation (43) can be expressed as

$$F_0(x) = e^{\lambda_1 x}\left[C_1 - \int_a^x dx' \frac{e^{\lambda_2 x'} Q(x')}{W(e^{\lambda_1 x'}, e^{\lambda_2 x'})}\right] + e^{\lambda_2 x}\left[C_2 + \int_a^x dx' \frac{e^{\lambda_1 x'} Q(x')}{W(e^{\lambda_1 x'}, e^{\lambda_2 x'})}\right], \quad (46)$$

where the expressions for $\lambda_{1,2}$ is given by Equation (45),

$$Q(x) = -\left(\frac{N_0}{4\pi p_0^3}\right)\frac{e^{-st_0}}{\kappa_0^I}\delta(x - x_0), \quad (47)$$

and the Wronskian

$$W(e^{\lambda_1 x}, e^{\lambda_2 x}) = e^{\lambda_1 x} e^{\lambda_2 x}(\lambda_2 - \lambda_1). \quad (48)$$

By requiring that $F_0(x)$ should be finite when $x \to \pm\infty$, expressions for C_1 and C_2 can be found so that solution (46) becomes

$$F_0(x, \eta, s) = -\left(\frac{N_0}{4\pi p_0^3}\right)\frac{e^{-st_0}}{\kappa_0^I}\frac{1}{\lambda_2 - \lambda_1} \times [e^{\lambda_1(x-x_0)}H(x_0 - x) + e^{\lambda_2(x-x_0)}H(x - x_0)], \quad (49)$$

where $\lambda_{1,2}$ is presented in Equation (45) and

$$\lambda_2 - \lambda_1 = -\left[\left(\frac{U_0^I - 2/3U_E^I\eta}{\kappa_0^I}\right)^2 - 4\left(\frac{D_0^I\eta^2 + (3D_0^I - 1/3\langle\nu_{\rm COM}^I\rangle)\eta - s(\tau_{\rm sc}^I s + 1) - 1/\tau_{\rm esc}}{\kappa_0^I}\right)\right]^{1/2}. \quad (50)$$

We do first the inverse Laplace transform

$$F_0(x, z, s) = \frac{1}{2\pi i}\int_{c-i\infty}^{c+i\infty} d\eta e^{z\eta} F_0(x, \eta, s), \quad (51)$$

after inserting the expression for $F_0(x, \eta, s)$ given by Equation (49). After completing the square of the second-order polynomial with respect to η in the square root of the expressions for $\lambda_{1,2}$ and $\lambda_2 - \lambda_1$ (see Equations (45) and (50)), these expressions become

$$\lambda_{1,2}(\eta, s) = \frac{1}{2}\frac{U_0^I}{\kappa_0^I} - \frac{1}{3}\frac{U_E^I}{\kappa_0^I}\eta \pm \sqrt{b^2(s) - \xi^2(\eta)},$$
$$\lambda_2(\eta, s) - \lambda_1(\eta, s) = -2\sqrt{b^2(s) - \xi^2(\eta)}, \quad (52)$$

where $b^2(s)$ and the new parameter $\xi^2(\eta)$ have the expressions

$$b^2(s) = \left(\frac{1}{2}\frac{U_0^I}{\kappa_0^I}\right)^2 + \frac{D_0^I}{\kappa_0^I}\left(\frac{q}{2}\right)^2\left(1 - \frac{1}{9}\frac{(U_E^I)^2}{\kappa_0^I D_0^I}\right) + \frac{1}{\kappa_0^I\tau_{\rm esc}} + \frac{1}{\kappa_0^I}s(\tau_{\rm sc}^I s + 1),$$
$$\xi^2(\eta) = \frac{D_0^I}{\kappa_0^I}\left(1 - \frac{1}{9}\frac{(U_E^I)^2}{\kappa_0^I D_0^I}\right)\left(\eta + \frac{q}{2}\right)^2, \quad (53)$$

and in $b^2(s)$

$$q = \left(3 - \frac{1}{3}\frac{\langle\nu_{\rm COM}\rangle - U_0^I U_E^I/\kappa_0^I}{D_0^I}\right)\Bigg/\left(1 - \frac{1}{9}\frac{(U_E^I)^2}{\kappa_0^I D_0^I}\right). \quad (54)$$

Accordingly, $F_0(x, z, s)$ can be expressed as

$$F_0(x, z, s) = \frac{1}{2}\left(\frac{N_0}{4\pi p_0^3}\right) \times \frac{e^{-st_0}}{\sqrt{\overline{D}_0^I\kappa_0^I}} e^{\frac{1}{2}\left(\frac{U_0^I}{\kappa_0^I} + \frac{1}{3}\frac{U_E^I}{\kappa_0^I}q\right)(x-x_0)}\left(\frac{p}{p_0}\right)^{-q/2} \times \frac{1}{2\pi i}\int_{c-i\infty}^{c+i\infty} d\xi e^{\left(\frac{z-(1/3)(U_E^I/\kappa_0^I)(x-x_0)}{\sqrt{\overline{D}_0^I/\kappa_0^I}}\right)\xi}\frac{1}{\sqrt{b^2 - \xi^2}} \times [e^{-(x_0-x)\sqrt{b^2-\xi^2}}H(x_0 - x) + e^{-(x-x_0)\sqrt{b^2-\xi^2}}H(x - x_0)], \quad (55)$$

where

$$\overline{D}_0^I = D_0^I\left(1 - \frac{1}{9}\frac{(U_E^I)^2}{\kappa_0^I D_0^I}\right). \quad (56)$$

By defining $\overline{\xi}^2 = -\xi^2$, the inverse Laplace transform in Equation (55) can be converted to a Fourier cosine transform so that

$$F_0(x, z, s) = \frac{1}{2}\left(\frac{N_0}{4\pi p_0^3}\right)\frac{e^{-st_0}}{\sqrt{\overline{D}_0^I\kappa_0^I}} e^{\frac{1}{2}\left(\frac{U_0^I}{\kappa_0^I} + \frac{1}{3}\frac{U_E^I}{\kappa_0^I}q\right)(x-x_0)}\left(\frac{p}{p_0}\right)^{-q/2} \times \frac{1}{\pi}\int_0^\infty d\overline{\xi}\cos\left(\left[\frac{z - (1/3)(U_E^I/\kappa_0^I)(x - x_0)}{\sqrt{\overline{D}_0^I/\kappa_0^I}}\right]\overline{\xi}\right) \times \left[\frac{e^{-(x_0-x)\sqrt{b^2+\overline{\xi}^2}}}{\sqrt{b^2 + \overline{\xi}^2}}H(x_0 - x) + \frac{e^{-(x-x_0)\sqrt{b^2+\overline{\xi}^2}}}{\sqrt{b^2 + \overline{\xi}^2}}H(x - x_0)\right]. \quad (57)$$

The Fourier cosine transform can be executed with the aid of transform (27) listed on page 17 of Erdelyi et al. (1954). We then find that

$$F_0(x, z, s) = \frac{1}{2\pi}\left(\frac{N_0}{4\pi p_0^3}\right)\frac{1}{\sqrt{\overline{D}_0^I\kappa_0^I}} \times \exp\left(\frac{1}{2}\left[\frac{U_0^I}{\kappa_0^I} + \frac{1}{3}\frac{U_E^I}{\kappa_0^I}q\right](x - x_0)\right)\left(\frac{p}{p_0}\right)^{-q/2} \times \exp(-st_0)K_0(db(s)), \quad (58)$$

where K_0 is the modified Bessel function of the second kind, which is a function of the parameters

$$d = \left[(x - x_0)^2 + \left(\frac{z - (1/3)(U_E^I/\kappa_0^I)(x - x_0)}{\sqrt{\overline{D}_0^I/\kappa_0^I}}\right)^2\right]^{1/2}, \quad (59)$$

$b(s)$ ($Re(b) > 0$) which is listed in Equation (53), and q which is given by Equation (54).

This is followed by doing the final inverse Laplace transform,

$$f_0(x, z, t) = \frac{1}{2\pi i}\int_{c-i\infty}^{c+i\infty} ds e^{st} F_0(x, z, s), \tag{60}$$

where $F_0(x, z, s)$ is specified according to Equation (58). Upon completing the square of the second-order polynomial with respect to s in the expression for $b(s)$ (Equation (53)) and after defining a new variable

$$\mu^2(s) = \frac{\tau_{\rm sc}^I}{\kappa_0^I}\left(s + \frac{1}{2\tau_{\rm sc}^I}\right)^2, \tag{61}$$

the solution for $f_0(x, z, t)$ becomes

$$\begin{aligned} f_0(x, z, t) = &\frac{1}{2\pi}\left(\frac{N_0}{4\pi p_0^3}\right)\frac{1}{\sqrt{\overline{D}_0^I \tau_{\rm sc}^I}} \\ &\times \exp\left(\frac{1}{2}\left[\frac{U_0^I}{\kappa_0^I} + \frac{1}{3}\frac{U_E^I}{\kappa_0^I} q\right](x - x_0)\right)\left(\frac{p}{p_0}\right)^{-q/2} \\ &\times \exp\left(-\frac{1}{2}\frac{t - t_0}{\tau_{\rm sc}^I}\right) \\ &\times \left[\frac{1}{2\pi i}\int_{c-i\infty}^{c+i\infty} d\mu e^{[\sqrt{\kappa_0^I/\tau_{\rm sc}^I}(t-t_0)]\mu} K_0(d\sqrt{\mu^2 - c^2})\right], \end{aligned} \tag{62}$$

where the expression for d can be found in Equation (59) and, in the limit of strong scattering,

$$\begin{aligned} c^2 = &\frac{\tau_{\rm sc}^I}{\kappa_0^I}\left(\frac{1}{2\tau_{\rm sc}^I}\right)^2 - \left(\frac{1}{2}\frac{U_0^I}{\kappa_0^I}\right)^2 \\ &- \frac{D_0^I}{\kappa_0^I}\left(\frac{q}{2}\right)^2\left(1 - \frac{1}{9}\frac{(U_E^I)^2}{\kappa_0^I D_0^I}\right) - \frac{1}{\kappa_0^I \tau_{\rm esc}} > 0. \end{aligned} \tag{63}$$

This implies a solution limit in which the scattering time is the shortest timescale. Thus, the scattering timescale is shorter than the effective diffusion timescale ($\tau_{\rm sc} < \tau_{\kappa_0^I} = \kappa_0^I/(U_0^I)^2$), the second-order Fermi acceleration timescale ($\tau_{\rm sc} < \tau_{D_0^I} = 1/D_0^I$), and the escape timescale ($\tau_{sc} < \tau_{\rm esc}$). The inverse Laplace transform in Equation (62) was performed using transform (47) on page 284 of Erdelyi et al. (1954), resulting in

$$\begin{aligned} f_0(x, p, t) = &\frac{1}{2\pi}\left(\frac{N_0}{4\pi p_0^3}\right)\frac{1}{\sqrt{\overline{D}_0^I \tau_{\rm sc}^I}} \\ &\times \exp\left(\frac{1}{2}\left[\frac{U_0^I}{\kappa_0^I} + \frac{1}{3}\frac{U_E^I}{\kappa_0^I} q\right](x - x_0)\right)\left(\frac{p}{p_0}\right)^{-q/2} \\ &\times \exp\left(-\frac{1}{2}\frac{t - t_0}{\tau_{\rm sc}^I}\right)\frac{\cosh(c\sqrt{v_c^2(t - t_0)^2 - d^2})}{\sqrt{v_c^2(t - t_0)^2 - d^2}} \\ &\times H(v_c(t - t_0) - d), \end{aligned} \tag{64}$$

where $v_c = \sqrt{\kappa_0^I/\tau_{\rm sc}^I} = v/\sqrt{3}$ is the collective speed of a nearly isotropic propagating particle pulse.

Solution (64) can be related to the Green's function solution for a point source of particles in space, time, and momentum according to the expression

$$G(x, x_0, p, p_0, t, t_0) = \left(\frac{4\pi p_0^2}{N_0}\right) f_0(x, p, t). \tag{65}$$

Then, the solution for a steady-state particle source given by

$$Q(x, p) = \left(\frac{dN_0/dt}{4\pi p_0^2}\right)\delta(x - x_0)\delta(p - p_0), \tag{66}$$

in which particles are injected at the fixed rate rate dN_0/dt into the SMFR acceleration region, can be found by integrating over the Green's function solution according to

$$\begin{aligned} f(x, p, x, t) = &\int_0^t dt_0' \int_{-\infty}^{\infty} dx_0' \\ &\times \int_0^{\infty} dp_0' G(x, x_0', p, p_0', t, t_0') Q(x_0', p_0'), \end{aligned} \tag{67}$$

which yields

$$\begin{aligned} f_0(x, p, t) = &\frac{1}{2\pi}\left(\frac{dN_0/dt}{4\pi p_0^3}\right)\frac{1}{\sqrt{\overline{D}_0^I \tau_{\rm sc}^I}} \\ &\times \exp\left(\frac{1}{2}\left[\frac{U_0^I}{\kappa_0^I} + \frac{1}{3}\frac{U_E^I}{\kappa_0^I} q\right](x - x_0)\right)\left(\frac{p}{p_0}\right)^{-q/2} \\ &\times \int_0^t d\tau \exp\left(-\frac{1}{2}\frac{\tau}{\tau_{\rm sc}^I}\right)\frac{\cosh(c\sqrt{(v_c\tau)^2 - d^2})}{\sqrt{(v_c\tau)^2 - d^2}} \\ &\times H(v_c\tau - d)H(p - p_0), \end{aligned} \tag{68}$$

where $\tau = t - t_0'$, $v_c = v/\sqrt{3}$,

$$\begin{aligned} \overline{D}_0^I &= D_0^I\left(1 - \frac{1}{9}\frac{(U_E^I)^2}{\kappa_0^I D_0^I}\right), \\ q &= \left(3 - \frac{1}{3}\frac{\langle \nu_{\rm COM}\rangle - U_0^I U_E^I/\kappa_0^I}{D_0^I}\right)\Bigg/\left(1 - \frac{1}{9}\frac{(U_E^I)^2}{\kappa_0^I D_0^I}\right), \\ c^2 &= \frac{\tau_{\rm sc}^I}{\kappa_0^I}\left(\frac{1}{2\tau_{\rm sc}^I}\right)^2 - \left(\frac{1}{2}\frac{U_0^I}{\kappa_0^I}\right)^2 - \frac{\overline{D}_0^I}{\kappa_0^I}\left(\frac{q}{2}\right)^2 - \frac{1}{\kappa_0^I \tau_{\rm esc}}, \\ d^2 &= (x - x_0)^2 + \frac{\kappa_0^I}{\overline{D}_0^I}\left[\ln\left(\frac{p}{p_0}\right) - \frac{1}{3}\left(\frac{U_E^I}{\kappa_0^I}\right)(x - x_0)\right]^2. \end{aligned} \tag{69}$$

ORCID iDs

J. A. Le Roux https://orcid.org/0000-0001-9199-2890
G. M. Webb https://orcid.org/0000-0002-0617-9502
O. V. Khabarova https://orcid.org/0000-0002-3230-2033
L.-L. Zhao https://orcid.org/0000-0002-4299-0490
L. Adhikari https://orcid.org/0000-0003-1549-5256

References

Adhikari, L., Khabarova, O. V., Zank, G. P., & Zhao, L.-L. 2019, ApJ, 873, 72
Adhikari, L., Zank, G. P., Bruno, R., et al. 2015, ApJ, 805, 63
Ambrosiano, J., Matthaeus, W. H., Goldstein, M. L., & Plante, D. 1988, JGR, 93, 14383
Bieber, J. W., Matthaeus, W. H., Smith, C. W., et al. 1994, ApJ, 420, 294
Birn, J., Hesse, M., & Schindler, K. 1989, JGR, 94, 241

Cartwright, M. L., & Moldwin, M. B. 2010, JGRA, 115, A08102
Dahlin, J. T., Drake, J. F., & Swisdak, M. 2016, PhPl, 23, 120704
Dahlin, J. T., Drake, J. F., & Swisdak, M. 2017, PhPl, 24, 092110
Dmitruk, P., Matthaeus, W. H., & Seenu, N. 2004, ApJ, 617, 667
Drake, J. F., Opher, M., Swisdak, M., & Chamoun, J. N. 2010, ApJ, 709, 963
Drake, J. F., Swisdak, M., Che, H., & Shay, M. A. 2006, Natur, 443, 553
Drake, J. F., Swisdak, M., & Fermo, R. 2013, ApJL, 763, L5
Du, S., Guo, F., Zank, G. P., Li, X., & Stanier, A. 2018, ApJ, 867, 16
Effenberger, F., & Litvinenko, Y. E. 2014, ApJ, 783, 15
Egedal, J., Daughton, W., Le, A., & Borg, A. L. 2015, PhPl, 22, 101208
Erdelyi, A., Magnus, W., Oberhettinger, F., & Tricomi, F. G. 1954, Table of Integral Transforms, Vol. 1 (New York: McGraw-Hill)
Eriksson, S., Newman, D. L., Lapenta, G., & Angelopoulos, V. 2014, PPCF, 56, 064008
Fu, H. S., Khotyaintsev, Yu. V., Vaivads, A., Retinò, A., & André, M. 2013, NatPh, 9, 426
Gosling, J. T., Skoug, R. M., Haggerty, D. K., & McComas, D. J. 2005, GeoRL, 32, L14113
Hu, Q., Zheng, J., Chen, Y., Le Roux, J. A., & Zhao, L. 2018, ApJS, 239, 12
Hunana, P., & Zank, G. P. 2010, ApJ, 718, 148
Khabarova, O. V., & Zank, G. P. 2017, ApJ, 843, 4
Khabarova, O. V., Zank, G. P., Li, G., et al. 2015, ApJ, 808, 181
Khabarova, O. V., Zank, G. P., Li, G., et al. 2016, ApJ, 827, 122
Khabarova, O. V., Zank, G. P., Malandraki, O. E., et al. 2017, SunGe, 12, 23
Lazarian, A., Vlahos, L., Kowal, G., et al. 2012, SSRv, 173, 557
Le Roux, J. A., Zank, G. P., & Khabarova, O. V. 2018, ApJ, 864, 158
Le Roux, J. A., Zank, G. P., Webb, G. M., & Khabarova, O. V. 2015, ApJ, 801, 112
Le Roux, J. A., Zank, G. P., Webb, G. M., & Khabarova, O. V. 2016, ApJ, 827, 47
Li, X., Guo, F., Li, H., & Birn, J. 2018, ApJ, 855, 80
Li, X., Guo, F., Li, H., & Li, G. 2015, ApJL, 811, L24
Li, X., Guo, F., Li, H., & Li, G. 2017, ApJ, 843, 21
Li, Y., & Lin, J. 2012, SoPh, 279, 91
Malandraki, O., Khabarova, O., Bruno, R., et al. 2019, ApJ, 881, 116
Malkov, M. A., & Sagdeev, R. Z. 2015, ApJ, 808, 15
Matthaeus, W. H., Ambrosiano, J. J., & Goldstein, M. L. 1984, PhRvL, 53, 1449
Matthaeus, W. H., Goldstein, M. L., & Roberts, D. A. 1990, JGR, 95, 20673
Morse, P. M., & Feshbach, H. F. 1981, Methods of Theoretical Physics (Minneapolis, MN: Feshbach)
Oka, M., Phan, T.-D., Krucker, S., Fujimoto, M., & Shinohara, I. 2010, ApJ, 714, 915
Shebalin, J. V., Matthaeus, W. H., & Montgomery, D. 1983, JPlPh, 29, 525
Smith, C. W., Isenberg, P. A., Matthaeus, W. H., & Richardson, J. D. 2016, ApJ, 638, 508
Weygand, J. M., Matthaeus, W. H., Dasso, S., & Kivelson, M. G. 2011, JGR, 116, A08102
Xia, Q., & Zharkova, V. 2018, A&A, 620, A121
Zank, G. P., Adhikari, L., Hunana, P., et al. 2017, ApJ, 835, 147
Zank, G. P., Hunana, P., Mostafavi, P., et al. 2015, JPhCS, 642, 012031
Zank, G. P., Le Roux, J. A., Webb, G. M., Dosch, A., & Khabarova, O. 2014, ApJ, 797, 28
Zank, G. P., & Matthaeus, W. H. 1992, JPlPh, 48, 85
Zank, G. P., & Matthaeus, W. H. 1993, PhFlA, 5, 257
Zhao, L.-L., Zank, G. P., Chen, Y., et al. 2019, ApJ, 872, 4
Zhao, L.-L., Zank, G. P., Khabarova, O. V., et al. 2018, ApJL, 864, L34
Zharkova, V., & Khabarova, O. 2012, ApJ, 752, 35
Zheng, J., & Hu, Q. 2018, ApJL, 852, L23